



UNIVERSIDAD DE CONCEPCIÓN
FACULTAD DE CIENCIAS FÍSICAS Y MATEMÁTICAS

Characterization of the PDR in LDN1622

POR CLAUDIO ANDRÉS RIVERA PIZARRO

Tesis presentada a la Facultad de Ciencias Físicas y Matemáticas de la
Universidad de Concepción para optar al grado de Magíster en Ciencias
con mención en Física.

PROFESOR GUÍA: RODRIGO ANDRÉS REEVES DÍAZ
AGOSTO, 2018
CONCEPCIÓN, CHILE

Characterization of the PDR in LDN1622

©CLAUDIO ANDRÉS RIVERA PIZARRO

Se autoriza la reproducción total o parcial, con fines académicos, por cualquier medio o procedimiento, incluyendo la cita bibliográfica del documento.



*Dedicado a mi familia,
por ellos, todo lo que soy*



Contents

List of Figures	VI
List of Tables	X
Abstract	XI
1 Introduction	1
1.1 1.1 Definitions of temperatures	1
1.1.1 1.1.1 Kinetic temperature	1
1.1.2 1.1.2 Excitation temperature	2
1.1.3 1.1.3 Brightness temperature	2
1.1.4 1.1.4 Rayleigh-Jeans temperature	2
1.1.5 1.1.5 Antenna temperature	2
1.1.6 1.1.6 Temperature of the main beam	2
1.2 1.2 Interstellar medium	3
1.2.1 1.2.1 Collisional Processes	5
1.2.1.1 1.2.1.1 Electron-Ion Inelastic Scattering	6
1.2.1.2 1.2.1.2 Ion-Neutral Collision Rates	6
1.2.1.3 1.2.1.3 Electron-Neutral Collision Rates	7
1.2.2 1.2.2 Radiative transfer	7
1.2.3 1.2.3 Photoionized gas	8
1.2.4 1.2.4 Nebular diagnostics	9
1.2.5 1.2.5 Interstellar dust	10
1.3 1.3 Coefficients of Einstein	10
1.3.1 1.3.1 Relation between A_{ul} , B_{ul} and B_{lu}	11
1.4 1.4 Usual mechanisms of emission	11
1.4.1 1.4.1 Free-Free	12
1.4.2 1.4.2 Synchrotron	12
1.4.3 1.4.3 Thermal	12
1.4.3.1 1.4.3.1 Thermal emission of dust	13
1.4.4 1.4.4 Fields of interstellar radiation in the vicinity of the sun	14
1.5 1.5 Origin of Fine-Structure lines	14
1.6 1.6 Molecular Line Spectra	16
2 Theoretical framework	19
2.1 2.1 Theoretical Basis	19

2.1.1	2.1.1 AME	19
2.1.1.1	2.1.1.1 Definition of AME emissivity	20
2.1.1.2	2.1.1.2 Other possibilities of AME	23
2.1.2	2.1.2 Dust grain	23
2.1.2.1	2.1.2.1 The original DL98 Model	25
2.2	2.2 State of the art	27
2.2.1	2.2.1 Objects of the interstellar medium	27
2.2.1.1	2.2.1.1 Molecular clouds	27
2.2.1.2	2.2.1.2 Warm ionized medium	28
2.2.1.3	2.2.1.3 Dark clouds	30
2.2.1.4	2.2.1.4 Reflection Nebulae	30
2.2.1.5	2.2.1.5 Photodissociation Regions	30
3	Observations and Data reductions	32
3.1	Observations	32
3.2	Data reductions	35
3.3	Results	37
3.4	A model of the physical and chemical structure of the LDN1622	43
4	Conclusion and Discussion	48
	Bibliography	52
	Appendix	58



List of Figures

1.1	Good approximation of an impact. There is a target and a projectile moving with respect to target with constant speed, b is the "impact parameter". Bruce T. Draine (2011)	5
1.2	Radiative transfer geometry. Bruce T. Draine (2011)	7
1.3	Neutral dust adjacent to an HII region, this region is called PDR. Typical SED of a PDR is shown in this figure with typical parameters as $EM = 4 \times 10^6 [cm^{-6}pc]$, $T = 3.5 \times 10^4 [K]$, near to star O8V. Bruce T. Draine (2011)	9
1.4	Continuous light given by four different temperatures. The graph follows Planck's function. ⁴	13
1.5	L and S generate sub-shells, which are seen as atomic fine-structure lines. And J is the total angular momentum operator.	16
1.6	Transitions of molecule of CO. CO(1-0) is the first excitation of this molecule and emits at the lowest frequency compared to the other transitions. When the density of the medium increases, the molecule can rotate with greater energy exiting its operator angular momentum to higher values. To de-excite emits radiation, this radiation has the frequencies shown in the figure (if they are not affected by redshift).	18
2.1	The grey body spectrum representing the thermal dust emission for a range of dust temperatures from 15 to 45 K with a fixed dust emissivity spectral index of 1.8. The $100[\mu m]$ emission (vertical dashed line) increases with increasing dust temperature.	22
2.2	The combination of free-free emission (dashed line) plus thermal emission(dot-dashed line) is inconsistent with the $33[GHz]$ signal shown here. Is necessary, consider an additional contribution (spinning dust). This is provided by different models of AME for electric dipole (ED (Draine and Lazarian, 1998)) and magnetic dipole (MD (Draine and Lazarian, 1990))	24
2.3	This figure show the angular moment plane and principle axis plane, using Euler angles we can describe an axisymmetric grain. (Hoang et al., 2010, 2011).	26
2.4	SED of RCW 175, with $\beta = 2$ and $T_d = 22.9[K]$. The data are fitting using three different scenarios. (a) Power-law radio emission plus thermal dust greybody. (b)Thermal bremsstrahlung with dust absorption plus thermal dust greybody. (c) Power-law radio emission plus spinning dust plus thermal dust greybody (Scaife, 2013)	29

2.5 Relative emissivity of microwave emission at 100 [μm] FIR emission as a function of molecular hydrogen column density, $N(H_2)$, for dark clouds. Clouds from (Scaife et al., 2009) and (Scaife, Hurley-Walker et al., 2009) are shown as filled circles, LDN 1622 (Casassus et al., 2006) is shown as filled stars, and LDN 1621 (Dickinson et al., 2010) is shown as a filled square. 31

3.1 The CSO consists of a 10.4[m] diameter Leighton telescope on Mauna Kea, Hawaii. A full complement of heterodyne receivers covers the atmospheric windows from 177 to 920[GHz]. The Surface accuracy is less than 15[$\mu m * r.m.s.$], pointing accuracy is 3[$arcsec * r.m.s.$] and its highest angular resolution is 8[$arcseconds$] 33

3.2 ASTE is located 4,800 meters above sea level, at the Atacama Desert in Northern Chile, it observes sub-millimeter (0.1[mm]-1[mm]) wavelengths. Telescope diameter is 10[m] and Beam size at 350 [GHz] is 22". 34

3.3 APEX is a 12-meter diameter telescope, operating at millimeter and sub-millimeter wavelengths between infrared light and radio waves. A beam of 18" at 345[GHz] CO(3-2) 34

3.4 In this window, the data reduction process is started. A mainly grade 1 polynomial baseline was used. Using the cursor, the range of the base line is marked. The x-axis was left in Km / s, and the y-axis was adjusted between -5 and 20 [K] for most spectra. This function generates two new files ending in .base and .base.his. Source: Our work. 35

3.5 In this figure LDN 1622 is shown at the corresponding frequency of the molecular transition of CO (3-2). The contours represent temperatures of 0.05[K], 2.54[K], 5.13[K], 7.73[K] and 10.32[K]. Source: Our work. 36

3.6 Above: On the left side there is a graphic representation of what a data cube is, each slice has spatial coordinates (RA, DEC) and represents a certain speed range. The set of all the slices is what we know as a data cube. On the right side we have the average spectrum of all the slices and all the pixels. You can see 3 broadcast peaks. Below: We zoom to the 3 peaks above and obtain from left to right graphs of temperature (K) v/s speed (km/s) of ^{13}CO , ^{12}CO and $C^{18}O$. To obtain the temperature graphs, you must select the desired speed ranges, as shown in the 3 graphs. Source: Our work. 36

3.7 This Figure shows the speed maps of LDN1622 at the frequencies of $^{13}CO(2-1)$ (Left) $C^{18}O(2-1)$ (Middle) and $CO(2-1)$ (Right) transitions. $^{13}CO(2-1)$ thin compared to $CO(2-1)$, so with $^{13}CO(2-1)$ we can observe deeper regions. However, the densest and most agglomerated nuclei can be seen with $C^{18}O(2-1)$, between the declinations $1^{\circ}40'00''$ and $1^{\circ}45'00''$ a very dense region is appreciated as well as near the declination $1^{\circ}50'00''$ and straight elevation $5^h54^m35^s$. Source: Our work. 37

3.8 Left: Temperature map of LDN1622 at 345[GHz]. Right: Temperature map of LDN1622 at 230[GHz], the green contours come from the emission of CO(3-2), with level steps of about 2.6[K]. The images shows a good spatial correlation. Source: Our work. 38

3.9 Left: Map of temperature of LDN1622 at the transitions of $C^{18}O(2-1)$. Right: Map of temperature of LDN1622, at the transition of $^{13}CO(2-1)$. $^{13}CO(2-1)$ is distributed evenly within the cloud, while $C^{18}O(2-1)$ begins to be noticed only in the interior regions. Source: Our work. 39

- 3.10 The final column density map of LDN1622 is displayed, only were considered regions where ^{13}CO and ^{12}CO were detected. Left: CO column density map. Right: H_2 column density map. Source: Our work. 40
- 3.11 UP: Maps obtained with APEX, on the left is the CO(4-3) temperature map and on the right the CI[P_1 - P_0] temperature map. DOWN: Both images correspond to the column density map of LDN1622, in the image on left the CO(4-3) contours are superimposed, in the image on the right side the CI[P_1 - P_0] contours are superimposed. Both quantities are spatially correlated because the radiation dissociates the CO molecule. Therefore probable to find neutral carbon in regions bordering on CO. Source: Our work. 41
- 3.12 Left: Image of LDN1622 observed at 461.040[GHz] with contours of neutral carbon emission. Right: Image of LDN1622 observed at 492.160[GHz] with contours of CO(4-3). Both images show a similar spatial correlation, in particular the distribution of CI within the LDN1622 is more homogeneous than the distribution of CO(4-3). Source: Our work. 42
- 3.13 Extinction map of LDN1622, produced by 2MASS NICER. The actual size of the pixel is approximately 0.7 times the FWHM, so we have about 1.4 arcmin per pixel. Source: Our work. 43
- 3.14 Meudon is a model that allows us to simulate the physical conditions of a PDR, is based on a stationary plane-parallel geometry of gas and dust illuminated by an ultraviolet (UV) radiation field coming from one or both sides of the cloud. In the left case, $\text{radp} = 0$ to not add the ISRF on the back side. 44
- 3.15 All panels are represented as function of the visual extinction, A_v . The first panel shows the proton density ($n(\text{H})+n(\text{H}_2)+n(\text{H}^+)$) and the total density ($n(\text{H})+n(\text{H}_2)+n(\text{He})$), both quantities become constant for high visual extinctions. The second panel represents the grain and gas temperature profiles. The blue area covers the range of dust temperature given by the MEUDON PDR Code for different grain size values in the range 0.03 to 0.3 μm . The third graph shows how the degree of ionization of the molecules varies depending on the extinction. Source: Our work. 45
- 3.16 The behavior of these 3 molecules was extracted from the Meudon model. In the graph above it shows the density of columns depending on the extinction. Around $A_v = 5$ the formation of CO is noted, but the abundance of C is even greater. For $A_v = 7$ the column density of CO is much greater than C, and almost equal to that of C+. Although for even greater extinctions the column density is much higher than the other two species, it is important to note that the column density of C continues to increase slowly while extinction increases. In the graph above we have the volumetric densities of the same chemical species. Precisely where C+ is decreasing and CO increasing, we find a peak in abundance of C, around $A_v = 4$. Source: Our work. 46
- 3.17 The same as Figure 3.15, but with $A_{v_{max}} = 10[\text{mag}]$. Source: Our work. 46
- 3.18 The same as Figure 3.16, but with $A_{v_{max}} = 10[\text{mag}]$. Source: Our work. 47

4.1 Left: Extinction map of LDN1622, all regions with magnitudes less than 3 and greater than 5 were eliminated. Right: Column density map of LDN1622, with contours that delimit visual extinctions between 3 and 5 magnitudes, obtained directly from the image above. The region between these limits is the probable PDR area. Source: Our work. 48

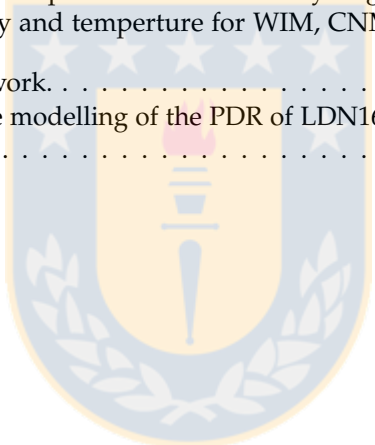
4.2 The figure shows the map of column density calculated in this work. Top-left: Contours at 160[μm]. Top-right: Contours at 250[μm]. Bottom-left: Contours at 350[μm]. Bottom-right: Contours at 500[μm]. Source: Our work. 50

4.3 Density of the H_2 column obtained from the Meudon model, both have the same input parameters, the only difference is that the graph on the left results from considering a maximum visual extinction of 30 magnitudes and the one on the left considers a maximum visual extinction of 10 Magnitudes. Both results show a maximum column density around 3×10^{21} . Source: Our work. 51



List of Tables

1.1	Here are listed the most critical characteristic of the different phases of the interstellar medium.	4
1.2	A denotes the total orbital angular momentum of the electrons in an atom. This table shows the different values and names that the angular momentum of an electron can take.	15
2.1	Sample of AME emissivity values, for AME detections in a variety of different environments computed relative at emission at $100 [\mu m]$	21
2.2	AME emissivity values computed relative to the hydrogen column density.	23
2.3	Typical values of density and temperture for WIM, CNM and WNM	28
3.1	Lines observed in this work.	33
3.2	Input parameters for the modelling of the PDR of LDN1622 using the Meudon PDR Code.	44



Abstract

The objective of this thesis is to physically characterize the Lynds Dark Nebula(LDN)1622. LDN1622 has been studied in infrared (IR) and ultraviolet (UV), and regions of low mass star formation have been contracted. In the microwave range, LDN1622 has also been observed and the results of these observations do not conform to galactic emission models in the vicinity of the Sun. For this reason, this work will plot the morphology of this cloud, to determine where you find the warm and dense nuclei and the transition zones. As future work, we want to compare these results with detailed observations in the microwave range.

To analyze the morphology of the cloud we analyzed molecular emission lines, these were $^{12}\text{CO}(2-1)$, $^{13}\text{CO}(2-1)$, $\text{C}^{18}\text{O}(2-1)$ taken with the APEX telescope, $^{12}\text{CO}(3-2)$ taken by the telescope ASTE, and $^{12}\text{CO}(4-3)$ and $\text{CI}[P_1 - P_0]$, both taken by the APEX telescope. With the cubes of data obtained by these emission lines, temperature and velocity maps of LDN1622 were made, with which it was possible to trace the densest nuclei, and the zones of transitions called PDR (photodissociation regions), and to make a molecular density map. To determine the PDR, we analyzed the Meudon PDR code, which is usually used to analyze the chemistry and physics of different interstellar clouds. From this model, neutral carbon information was extracted and used as PDR tracer, which made possible to establish a relationship between neutral carbon and visual extinction. Once we could establish the visual extinction where we expect to find PDR, we compared our results with a LDN1622 visual extinction map produced by NICER and with the column density map.

It was found that the density of LDN1622 should be less than $10^5[\text{cm}^{-3}]$. PDR was estimated precisely in the contours of the density map of LDN1622, this agrees with the idea that the UV radiation of nearby stars does not manage to penetrate the cloud, and this transition zone is established, between a molecular region and an atomic region. As in the neighborhoods, similar morphologies were found for CI and CO(4-3), which suggests that although the PDR is a transition zone, the cloud is sufficiently porous to allow part of the UV radiation to penetrate the cloud and dissociate molecules.

Chapter 1

Introduction

In this chapter, we discuss topics related to the interstellar medium.

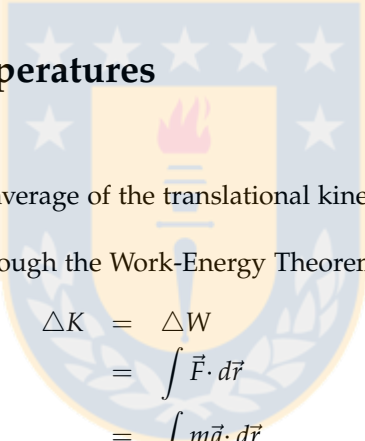
The interstellar medium can be studied (among other things) by the radiation that reaches the Earth. Therefore, understanding the physical mechanisms responsible for radiation, whether through the continuum, emission or absorption lines, is very important.

1.1 Definitions of temperatures

1.1.1 Kinetic temperature

Is the temperature given by the average of the translational kinetic energy of particles, it appears in the law of an ideal gas.

The kinetic energy is defined through the Work-Energy Theorem:


$$\begin{aligned}\Delta K &= \Delta W \\ &= \int \vec{F} \cdot d\vec{r} \\ &= \int m\vec{a} \cdot d\vec{r} \\ &= m \int \frac{d\vec{v}}{dt} \cdot d\vec{r} \\ &= m \int \frac{d\vec{r}}{dt} \cdot d\vec{v} \\ &= m \int \vec{v} \cdot d\vec{v} \\ &= \frac{1}{2}mv^2 - \frac{1}{2}mv_0^2\end{aligned}$$

Typically, initial velocity v_0 is set to 0. So the kinetic energy is

$$\Delta K = \frac{1}{2}mv^2 \tag{1.1.1}$$

1.1.2 Excitation temperature

The relationship between two populations and two levels of energy, involved in the transition, is given by the Boltzmann law by the temperature that defines the thermodynamic equilibrium.

$$\frac{n_1}{n_2} = \frac{g_1}{g_2} e^{\frac{h\nu_{21}}{kT_{ex}}} \quad (1.1.2)$$

In other words the excitation temperature is equal to the kinetic temperature in the limit of thermodynamic equilibrium.

1.1.3 Brightness temperature

Is a property of a radiating body connected to its a specific intensity of emission. Is equal to the temperature of an ideal black body, that it should emit that same intensity.

$$I_\nu = \frac{2h\nu^3}{c^2} \frac{1}{e^{\frac{h\nu}{kT_B}} - 1} \quad (1.1.3)$$

1.1.4 Rayleigh-Jeans temperature

Also called radiation temperature.

$$I_\nu = \frac{2kT\nu^2}{c^2} \quad (1.1.4)$$

The brightness temperature converges to Rayleigh-Jeans temperature for long wavelengths, in the equation 1.1.3 (to long wavelengths) we have that $h\nu \ll kT$, so the denominator can be written as $\exp(\frac{h\nu}{kT}) - 1 = \frac{h\nu}{kT} + \dots$; despise the other terms. With this simple approach we have Rayleigh-Jeans temperature.

1.1.5 Antenna temperature

The power received from an antenna, expressed as temperature

$$P_{source} = kT_A \Delta\nu \quad (1.1.5)$$

or expressed in terms of flux.

$$T_A = \frac{A}{2k} F_\nu \eta_A \quad (1.1.6)$$

where η_A is the antenna efficiency

1.1.6 Temperature of the main beam

It is the antenna temperature corrected for the telescope efficiency.

$$T_{mb} = \frac{T_A}{\eta_A} \quad (1.1.7)$$

The temperature of the main beam and radiation temperature are equal when the source is resolved

$$T_{mb} = T_r \frac{\Omega_{source}}{\Omega_{beam}} \quad (1.1.8)$$

1.2 Interstellar medium

The interstellar medium (ISM) is the most important component in the Milky Way (MW), because is the place where stars are born. With the evolution of galaxies the ISM is transformed into stars, sometimes the ISM can disappear, it is known in Giant Ellipticals. Despite the importance of ISM, it represents only 10% of MW, and is composed by

- Interstellar dust (Small particles whose size is less than $1[\mu m]$).
- Interstellar gas (ions, atoms and molecules in the gas phase. The distribution of velocity is near to the thermal).
- Dark matter (Unknown particles whose interactions remain speculative).
- Cosmic rays (Ions and electrons with relativistic energies at $10^{21}[eV]$).
- Gravitational field (due to all matter in the galaxy).
- Interstellar magnetic fields (due to electron currents).
- Electromagnetic radiation (CMB, stellar atmospheres, radiation of ions, atoms and molecules, thermal emission, free-free emission, Synchrotron emission, gamma rays).

The total mass of the MW (in a radius of $15[kpc]$) is about 10^{12} solar masses. To give typical values the 10% is baryonic matter and the 90% should be dark matter; and only the 10% of baryonic matter is gas, hydrogen and helium mainly. The amount of hydrogen is much higher than that of helium, therefore hydrogen is the most important element of the ISM. The 60% of the Hydrogen of ISM in the MW is in the form of HI, the 20% is in the form of H_2 and the 20% in the form of HII. The star formation lies in a thin disk in the MW, this disk is composed of gas and dust with a thickness of a few parsecs and it is symmetrical with respect to the galactic plane.

But the ISM is dynamic, it can manifest in different phases. Those phases are divided in 7 phases called Coronal gas, HII gas, Warm HI, Cool HI, Diffuse molecular gas, Dense molecular cloud and Stellar winds; in simple words those phases represents different temperatures and density.

Coronal gas

Gas with temperature $\geq 10^{5.5}[K]$. This gas is heated by supernova waves. It is ionized by ions such as O [VI]. It is a gas with low density and it is often called hot ionized medium (HIM), see the Table 1.1.

HII gas

Gas with temperature $\geq 10^4[K]$. Is a gas where H is photoionized by UV photons, from hot stars. Due to its high density this region is called HII region, but when the density is low this region is called warm ionized medium (WIM), see the Table 1.1.

Warm HI

Atomic gas with temperature $T \geq 10^{3.7}[K]$ and density of $n_H \geq 0.6[cm^{-3}]$, is often called warm neutral medium (WNM), see the Table 1.1.

Cold HI

Atomic gas at a temperature $\geq 10^2[k]$ with density $n_H \geq 30[cm^{-3}]$, often called cold neutral medium (CNM), see the Table 1.1.

Diffuse molecular gas

Typical temperature $T \geq 50[K]$, is similar to Cold HI, but with high density; this causes that Hydrogen is formed in its interior. See the Table 1.1.

Dense molecular cloud

Temperature at $T \sim 10 - 50[k]$ and density $n_H \geq 10^3[cm^{-3}]$, often called dark nebula with visual extinction $A_v \geq 3[mag]$ in its interior. Here the dust grains are coated with water and other ice molecules. See the Table 1.1.

Stellar winds

Stellar winds cause stars to lose mass, with velocities up to $30[km/s]$, temperatures of $50 - 10^3[K]$ observed in the Optic, UV, IR, HI, CO, OH emission.

Table 1.1: Here are listed the most critical characteristic of the different phases of the interstellar medium.

Phases	It is cooled by	It is warmed by	Is observed by
Gas coronal	Adiabatic expansion and x-ray emission	Collision ionization	UV, radio, x-ray emission synchrotron emission
HII gas	Optic, free-free, and fine structure emission	Photoelectrons of H and He (photoionization)	Optic and thermal emission in pressure equilibrium
Warm HI	Optical and fine structure emission	Photoelectrons of dust	[HI], Absorption of UV and optical
Cool HI	Fine structure emission	Photoelectrons of dust	[HI]
Diffuse molecular gas	Fine structure emission		[HI], and absorption of CO, optic and UV
Dense molecular cloud	CO and [CI]	Photoelectrons of dust	CO and emission of dust (IR)

The ISM is far from thermodynamic equilibrium, and it is able to keep this state due to the input of free energy. Mainly this free energy is UV radiation from stars and kinetic energy from supernovae. In simple words, non-thermodynamic equilibrium in the ISM means that it does not radiate as a black body, so it does not radiate according to its temperature. For example, every collisional excitation is followed by radioactive decay, and these types of processes impede the thermodynamic equilibrium. Keeping this, the valid distribution in the ISM is the Maxwell distribution of velocities, given by

$$f(v)dv = \frac{4}{\sqrt{\pi}} \left(\frac{m}{2kT}\right)^{\frac{3}{2}} v^2 e^{-\frac{v^2 m}{kT}} dv$$

where m is the mass of the particle, k is the Boltzmann constant, T is the temperature, v is the velocity. The elastic collisions are sufficiently frequent to thermalize the velocity distribution. Also,

the interstellar medium is a region where statistical balance can be assumed, between levels of population in a certain energy "i" and levels of population in another energetic level "j", therefore it is fulfilled that

$$\frac{dn_i}{dt} = \sum_j (-R_{ij}n_i + R_{ji}n_j) = 0$$

Where "n" is the number of particles in that state, and "R" transition of radioactive processes. But in the other hand distribution like the Boltzmann and Planck are not valid, since $T_{kin} \neq T_{ex}$.

1.2.1 Collisional Processes

The reason that the ISM is treated as a fluid is due to collisions between particles, this result in the emission of photons. Collisions depend on the density and temperature of the medium, and obviously the velocity distribution function for the particles will be close to a Maxwellian distribution.

For two-body collisional process the reaction rate per unit volume is $n_A n_B \langle \sigma(v) \rangle_{AB}$, where $\langle \sigma(v) \rangle$ is the collisional rate coefficient (to particles A and B), and is given by

$$\langle \sigma(v) \rangle_{AB} \equiv \int_0^\infty \sigma_{AB}(v) v f_v dv \quad (1.2.1)$$

In the last equation $\sigma_{AB}(v)$ is the velocity-dependent reaction cross section, $f(v)dv$ is the probability that A and B have a relative velocity v in dv . It is possible to give an algebraic approximation for the collisions.

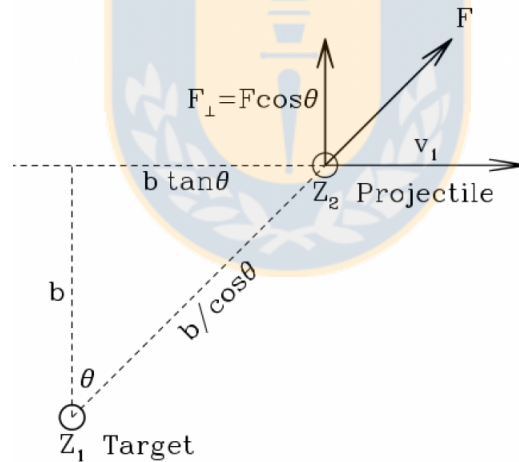


Figure 1.1: Good approximation of an impact. There is a target and a projectile moving with respect to target with constant speed, b is the "impact parameter". Bruce T. Draine (2011)

Assuming that the projectile and target velocities remain constant during the encounter, there is an exchange of momentum between projectile and target. The force perpendicular to the trajectory

between particles with charges Z_1e and Z_2e is given by

$$F_{\perp} = \frac{Z_1 Z_2 e^2}{\left(\frac{b}{\cos(\theta)}\right)^2} \cos(\theta) \quad (1.2.2)$$

$$= \frac{Z_1 Z_2 e^2}{b^2} \cos^3(\theta) \quad (1.2.3)$$

For equation 1.2.2 it is necessary to consider the figure 1.1. The parameter b is the distance of closest approach if the projectile were to travel undeflected. In Figure 1.1 v_1 is the relative velocity, so

$$dt = \frac{d(btg(\theta))}{v_1} \quad (1.2.4)$$

$$= \frac{b}{v_1} \frac{d\theta}{\cos^2(\theta)} \quad (1.2.5)$$

To calculate the momentum transfer the classic definition is used, see the equation 1.2.6

$$\Delta p_{\perp} = \int_{-\infty}^{\infty} F_{\perp} dt \quad (1.2.6)$$

$$= \frac{Z_1 Z_2 e^2}{bv_1} \int_{-\frac{\pi}{2}}^{\frac{\pi}{2}} \cos(\theta) d\theta \quad (1.2.7)$$

$$= 2 \frac{Z_1 Z_2 e^2}{bv_1} \quad (1.2.8)$$

1.2.1.1 Electron-Ion Inelastic Scattering

This kind of collision (and emission line) is present from HII regions to supernova remnants. The basic scheme is a collision between an ion and an electron (attracted by the Coulomb potential), this collision leaves the ion in an excited state, from which it will decay emitting a photon. In the case when the ion is excited to a state u , the thermally averaged rate coefficient for de-excitation to a lower energy level l can be written in terms of a dimensionless quantity called "collision strength" (Ω_{ul}) as

$$\langle \sigma v \rangle_{u \rightarrow l} \equiv \frac{h^2}{(2\pi m_e)^{\frac{3}{2}}} \frac{1}{(kT)^{\frac{1}{2}}} \frac{\Omega_{ul}(T)}{g_u} \quad (1.2.9)$$

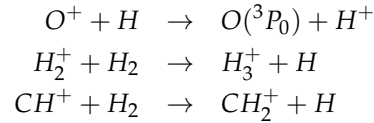
$$\equiv \frac{8.629 \times 10^{-10}}{\sqrt{T}} \frac{\Omega_{ul}}{g_u} [cm^3 s^{-1}] \quad (1.2.10)$$

where g_u is the electrical degeneration. The collision strength is a function of temperature, but the theory (in quantum-mechanics) show that Ω_{ul} is independent of temperature for $T \leq 10^4 [K]$ and typically have values in the range 1 to 10.

1.2.1.2 Ion-Neutral Collision Rates

In this case, the situation is the interaction between charged particles and neutral particles, if their separation is more than a few \AA the neutral particle is polarized due to the electric field

of the ion. The ion has an electric charge of Ze and the neutral particle has a polarizability α_n . For the magnetic field to remain constant, it is required an electric dipole moment $\vec{P} = \alpha_N \vec{E}$. The polarizability of atoms is of order a few a_0^3 , where $a_0 \equiv \frac{\hbar^2}{m_e e^2} = 5.292 \cdot 10^{-9} [cm]$ is the Bohr radius. Examples of those exothermic reactions include



1.2.1.3 Electron-Neutral Collision Rates

Regions with low ionization rate have a strong electron-neutral scattering, in this case the primary collision is H_2 , followed by He . At energies $E < 0.044[eV]$ the scattering is purely elastic, for $E > 0.044[eV]$, rotational excitation can occur; at $E \geq 0.5[eV]$ vibrational excitation is also possible and for $E > 11[eV]$ electronic excitation can take place. Collisions are much more likely to occur with H_2 because the cross section for electron scattering by He is smaller than that for H_2 .

1.2.2 Radiative transfer

The equation of radiative transfer describes the propagation of radiation through absorbing and emitting media. See Figure 1.2.

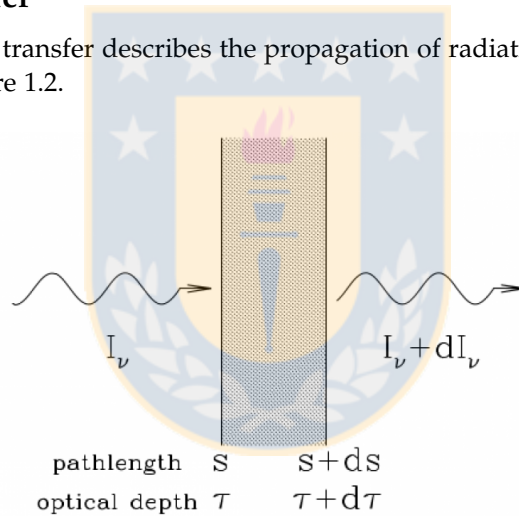


Figure 1.2: Radiative transfer geometry. Bruce T. Draine (2011)

The specific intensity I_ν is the amount of energy per units of area, time, frequency and solid angle. In thermal equilibrium, the intensity is given by

$$I(\nu, \vec{n}, \vec{r}, t) = \frac{dE_\nu}{dA \cos(\theta) dt d\nu d\Omega} \quad (1.2.11)$$

$$= \frac{2h\nu^3}{c} \frac{1}{e^{\frac{h\nu}{kT}} - 1} \quad (1.2.12)$$

It is useful specific energy density u_ν given by

$$u_\nu = \frac{1}{c_m} \int I_\nu d\Omega$$

where c_m is the speed of light in the medium.

Let "s" the measure path length along the direction of propagation, so the equation of radiative transfer is

$$dI_\nu = -I_\nu \kappa_\nu ds + j_\nu ds \quad (1.2.13)$$

The first term is the total change of I_ν due to the absorption and stimulated emission. The second term is the change of I_ν due to spontaneous emission by the material. In the last equation, there are two coefficients, κ_ν is the attenuation coefficient at frequency ν , and j_ν coefficient of emissivity at frequency ν .

The radiative transfer can be written in terms of the optical depth which is defined by

$$d\tau_\nu \equiv \kappa_\nu ds \quad (1.2.14)$$

So, the radiative transfer is

$$dI_\nu = -I_\nu d\tau_\nu + S_\nu d\tau_\nu \quad (1.2.15)$$

where $S_\nu = \frac{j_\nu}{\kappa_\nu}$ is a source function.

Working with the equation 1.2.15, the radiative transfer equation can be written in an integral way, this is

$$dI_\nu + I_\nu d\tau_\nu = S_\nu d\tau_\nu \quad (1.2.16)$$

$$e^{\tau_\nu} (dI_\nu + I_\nu d\tau_\nu) = e^{\tau_\nu} S_\nu d\tau_\nu \quad (1.2.17)$$

$$d(e^{\tau_\nu} I_\nu) = e^{\tau_\nu} S_\nu d\tau_\nu \quad (1.2.18)$$

$$e^{\tau_\nu} I_\nu - I_\nu(0) = \int_0^{\tau_\nu} e^{\tau'_\nu} S_\nu d\tau'_\nu \quad (1.2.19)$$

$$e^{\tau_\nu} I_\nu - I_\nu(0) = \int_0^{\tau_\nu} e^{\tau'_\nu} S_\nu d\tau'_\nu \quad (1.2.20)$$

$$(1.2.21)$$

1.2.3 Photoionized gas

There are stars (OB) which produce a flux of photons with energy higher than the binding potential between the H-nucleus and its electron, therefore a photoionized gas is formed around the star. The star ionizes the HI is forming an HII-region called sphere of Stromgren, given by

$$R_s = 9.77 \times 10^{18} \left(\frac{Q_0}{10^{49}} \right)^{\frac{1}{3}} n_2^{-\frac{2}{3}} T_4^{0.28} [cm]$$

For stars with $T < 5000[K]$ the ionizing photons have an energy of $\sim 18[eV]$ and its cross-section is $\sigma = 2.95 \times 10^{-8} [cm^2]$. The mean free path is

$$mfp = \frac{1}{n(H)\sigma} = 3.39 \times 10^{17} \left[\left(\frac{cm^{-3}}{n(H)} \right) cm \right]$$

For a typical value of Q_0 (Ionizing photon ratio), the mfp is much smaller than R_s . In other words, the transition zone between the sphere of Stromgren and HI is very small. Radiation in the vicinity of hot stars is given by Figure 1.3.

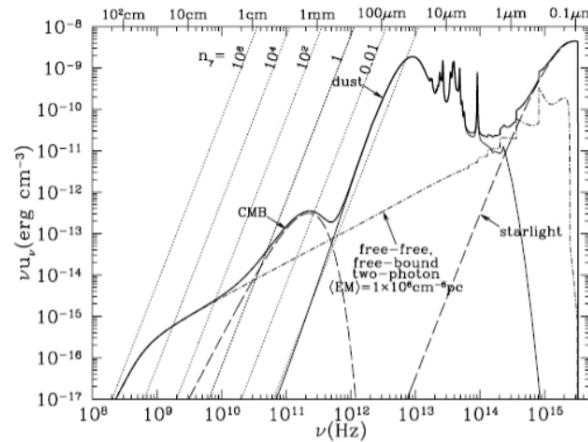


Figure 1.3: Neutral dust adjacent to an HII region, this region is called PDR. Typical SED of a PDR is shown in this figure with typical parameters as $EM = 4 \times 10^6 [cm^{-6} pc]$, $T = 3.5 \times 10^4 [K]$, near to star O8V. Bruce T. Draine (2011)

All energy photons between 13.6 and 100 [eV] are absorbed by this HII region. Radiation with energy, lower than 13.6 [eV] leaves this region absorbed only by the dust. When leaving this region, the photons enter the region of photodissociation (PDR) where the molecules are dissociated by the photons.

1.2.4 Nebular diagnostics

The population of the excited levels of the atoms depends on the electron density and temperature. So we can use atoms and their radiation to estimate the temperature and density of the ISM. There are two kinds of diagnostics:

- The first uses atoms that have two energy levels that differ an amount of energy comparable to the thermal energy kT of the gas.
- The second uses atoms that have two energy levels that have almost the same energy.

The most important processes that cool a HI cloud are the emission lines of the C and O. Another cooling process can be produced by a collision, where the energy is transferred to the particle that collides instead of being emitted as electromagnetic energy. In this case the gas does not cool. Since the density in a cloud is very low, the probability of a collision between particles is negligible.

1.2.5 Interstellar dust

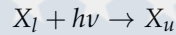
Interstellar dust grains have their origin in the material ejected by stars, it contains a large amount of carbon and silicon atoms, producing visual extinction and thermal emission. Dust plays a very important role in the evolution of the Galaxy, helps in the formation of complex molecules, heats the gas by means of the emission of photoelectrons, and in dense regions its infrared emission is a very important cooling mechanism.

But there are different types of dust grains, with different compositions, size and shape.

- In composition, they are composed of carbonaceous, silicate and/or metallic.
- In shape, are spherical, spheroidal, fractal, disk/sheetlike (expected for polycyclic aromatic hydrocarbons) and needle-like. Even with formation of ice mantles.
- In size, smaller than $100[\mu m]$.

1.3 Coefficients of Einstein

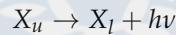
The atoms in the ISM, can absorb photons and achieve a higher energy state. If l is the state with less energy, and u is the state with more energy. The absorption is described by



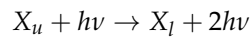
This introduces an inversely proportional relationship between both populations (u and l) given by

$$\left(\frac{dn_u}{dt}\right)_{l \rightarrow u} = -\left(\frac{dn_l}{dt}\right)_{l \rightarrow u} = n_l B_{lu} u_\nu$$

where n is the number density, u_ν is the radiation energy density per unit frequency, and B_{lu} is the Einstein coefficient for the transition $l \rightarrow u$. The atom in an excited level u , (spontaneously or stimulated) can emit a photon decaying to a lower level. For spontaneous emission



and for stimulated emission



The spontaneous emission is a random process, is independent of the presence of a radiation field. This random process has a probability per unit time given by the Einstein A coefficient A_{ul} . Stimulated emission occurs with a photon with identical frequency, polarization and direction of propagation. Therefore the total rate of depopulation of level u due to emission of photons, can be written as

$$\left(\frac{dn_l}{dt}\right)_{u \rightarrow l} = -\left(\frac{dn_u}{dt}\right)_{u \rightarrow l} = n_u (B_{ul} u_\nu + A_{ul})$$

Where B_{ul} is the Einstein B coefficient for the downward transition $u \rightarrow l$ and u_ν is the energy density of the radiation surrounding the atom.

1.3.1 Relation between A_{ul} , B_{ul} and B_{lu}

The specific energy density in thermal equilibrium is

$$(u_\nu)_{LTE} = \frac{4\pi}{c} B_\nu(T) \quad (1.3.1)$$

$$= \frac{8\pi h\nu^3}{c^3} \frac{1}{e^{\frac{h\nu}{kT}} - 1} \quad (1.3.2)$$

To a blackbody radiation field, the net rate of change of level u is

$$\begin{aligned} \frac{dn_u}{dt} &= \left(\frac{dn_u}{dt}\right)_{l \rightarrow u} + \left(\frac{dn_u}{dt}\right)_{u \rightarrow l} \\ &= n_l B_{lu} \frac{8\pi j\nu^3}{c^3} \frac{1}{e^{\frac{h\nu}{kT}} - 1} - n_u \left(A_{ul} + B_{ul} \frac{8\pi h\nu^3}{c^3} \frac{1}{e^{\frac{h\nu}{kT}} - 1} \right) \end{aligned}$$

In Thermodynamic equilibrium

$$0 = \frac{dn_u}{dt} \quad (1.3.3)$$

$$= \left(\frac{dn_u}{dt}\right)_{l \rightarrow u} + \left(\frac{dn_u}{dt}\right)_{u \rightarrow l} \quad (1.3.4)$$

$$= n_u B_{lu} u_\nu - (n_u A_{ul} + n_u B_{ul} u_\nu) \quad (1.3.5)$$

$$\Rightarrow n_u B_{lu} u_\nu = (n_u A_{ul} + n_u B_{ul} u_\nu) \quad (1.3.6)$$

$$\frac{u_\nu (n_l B_{lu} - n_u B_{ul})}{n_l B_{lu} - n_u B_{ul}} = \frac{n_u A_{ul}}{n_l B_{lu} - n_u B_{ul}} \quad (1.3.7)$$

$$\Rightarrow u_\nu = \frac{\frac{A_{ul}}{B_{ul}}}{\frac{n_l B_{lu}}{n_u B_{ul}} - 1} \quad (1.3.8)$$

from equation 1.1.2, it is known that

$$u_\nu = \frac{\frac{A_{ul}}{B_{ul}}}{\frac{g_l B_{lu}}{g_u B_{ul}} e^{\frac{h\nu}{kT}} - 1}$$

and comparing terms with equation 1.3.1, the following expression is obtained

$$B_{ul} = \frac{c^3}{8\pi h\nu^3} A_{ul}$$

and from $g_l B_{lu} = g_u B_{ul}$ the other Einstein coefficient is

$$B_{lu} = \frac{g_u}{g_l} \frac{c^3}{8\pi h\nu^3} A_{ul}$$

1.4 Usual mechanisms of emission

The usual mechanisms of emission from galactic background are Free-free, thermal and synchrotron. These mechanisms of emissions produce energy in most of the electromagnetic spectrum.

1.4.1 Free-Free

This kind of emission is often produced by free electrons scattering. Consider three scenarios identical particles, electron-electron and electron-ion interaction. Interactions between identical particles often do not radiate significantly, because the accelerations of two particles has equal magnitude but opposite direction, so their radiated electric field are equal magnitude but opposite in sign. The radiation from electron-electron collision will be ignored for the same reason. In an electron-ion collision, the electron will therefore radiate at least $(\frac{m_p}{m_e})^2 \approx 4 \cdot 10^6$ as much power as the ion (with m_p is the ion mass and m_e is the electron mass), so we may neglect the radiation from all of the ions and we will assume that the energy lost by an electron when it interacts with an ion is much smaller than the initial electron energy. In conclusion *"Only electron-ion collisions are important and only the electrons radiate significantly"*³.

Just electrons are considered like charged particles responsible of free-free emission, and emit radio radiation because are accelerated electrostatically following to Larmor's formula

$$E_{\perp} = \frac{q\ddot{v}\sin(\theta)}{rc^2} \quad (1.4.1)$$

where q is charge, θ is the angle between the acceleration \ddot{v} and the line-of-sight of the observer, c is the speed of light and r is the distance. Radio free-free emission is expected to manifest from any environment populated by an ionized plasma.

1.4.2 Synchrotron

When an electron is accelerated due to a magnetic field this emit radiation that is known as synchrotron radiation. Is a radiation strongly polarized, where the electron moves close to the speed of light. The power of just one electron can be described by the Larmor's formula, see equation 1.4.2 in an inertial frame in which the electron is instantaneously at rest.

$$P = \frac{2}{3} \frac{m_e r_e a^2}{c} \quad (1.4.2)$$

Where a is the acceleration, and r_e is the classical electron radius. But is necessary Lorentz transform to calculate the power these results to the frame of an observer at rest in the Galaxy where the effects of general relativity cannot be despised. In this case the average power is given by

$$\langle P \rangle = \frac{4}{3} \sigma_T \gamma^2 \beta^2 c U_B \quad (1.4.3)$$

Where $\beta = \frac{v}{c}$, $\sigma_T \equiv \frac{8\pi}{3} (\frac{e^2}{m_e c^2})^2$ called Thomson cross section, the magnetic energy density is $U_B = \frac{B^2}{8\pi}$, $\gamma \equiv (1 - \beta^2)^{-\frac{1}{2}}$, c is the speed of light.

1.4.3 Thermal

All matter with a temperature greater than absolute zero emits thermal radiation. The frequency distribution is given by Planck's law of black-body radiation for an idealized emitter, see Figure 1.4.

³ <http://www.cv.nrao.edu/course/ast534/FreeFreeEmission.html>

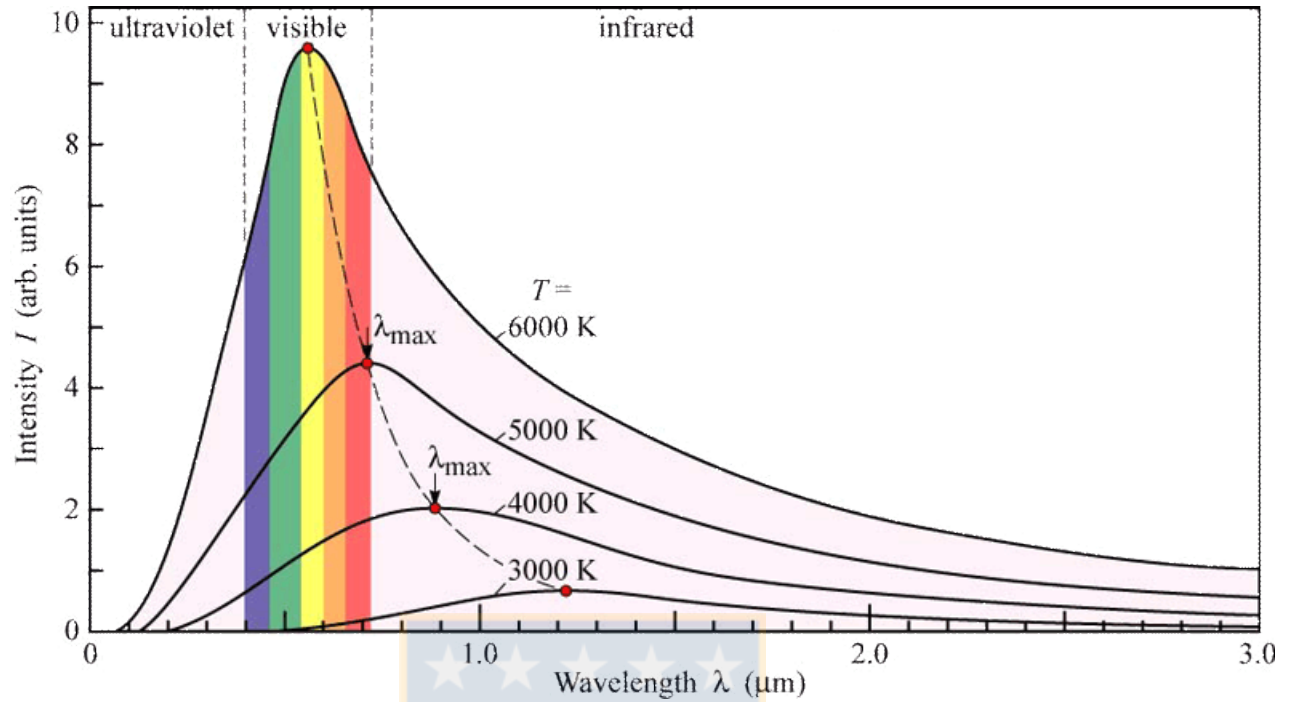


Figure 1.4: Continuous light given by four different temperatures. The graph follows Planck's function. ⁴

Planck's law is given by equation 1.4.4, introducing the Planck's constant $h = 6.6260693 \times 10^{34} [Js]$

$$I_\nu = \frac{2h\nu^3}{c^2} \frac{1}{e^{\frac{h\nu}{kT_B}} - 1} \quad (1.4.4)$$

T_B is Brightness temperature

1.4.3.1 Thermal emission of dust

The emission of dust grain is approximately expressed by

$$S_\nu \propto \nu^{\frac{2+\beta}{1+\Delta}} B_\nu(T_d) \quad (1.4.5)$$

In figure 2.1 from (Tibbs et al., 2012) there is a spectrum of emission dust. In this case, β is the opacity index, opacity is $\kappa_\nu = \kappa_0 \left(\frac{\nu}{\nu_0}\right)^\beta$ (Hildebrand, 1983), ν is the frequency, T_d is the dust temperature, B_ν is the Planck function and S_ν is the flux density.

β depends of the composition, size and distribution of the dust. The smaller grains a have higher opacity index (Scaife, 2013).

$$\beta = (1 + \Delta)(\alpha - 2)$$

⁴ <http://motls.blogspot.cl/2010/04/on-importance-of-black-bodies.html>

β is related to α (flux density index) and Δ that is the ratio of optically thick to optically thin emission and decreases at longer wavelengths. Has been observationally determined in the region $350[\mu m]$ to $1.3[\mu m]$ for dark clouds as $\Delta \simeq 0.2$ (Rodmann et al., 2006; Lommen et al., 2007). $\beta \sim 0$ is proposed for the tail of the spectrum of a grey body, usually for young stellar objects which are dominated by dust grain. For diffuse interstellar medium $\beta \approx 1.8 - 2$. For grains with a size distribution $\frac{dn}{da} \propto a^p$, where the grain size $a \leq a_{max}$ and $a_{max} \geq 3\lambda$, where λ is the wavelength of observation, the measured opacity index will be

$$\beta(\lambda) \approx (p - 3)\beta_{ISM} \quad (1.4.6)$$

Typically the power-law index is $p = 3.5$ (Mathis et al., 1977), grains with $\beta_{ISM} \approx 2$ will have $\beta \approx 1$ when $a_{max} \geq \lambda$ and by extension $\beta \leq 1$ when $a_{max} > 3\lambda$ (Draine, 2006); $p = 3$ for protoplanetary disks (Tanaka et al., 2005) and β is even smaller.

The contribution at microwave frequencies ($\lambda > 3[mm]$) is expected to come from the largest grains. From (Draine and Lazarian, 1998) and (Boulanger and Perault, 1988) is known that the rotational emission of the small grain has no effect on the grey-body tail.

1.4.4 Fields of interstellar radiation in the vicinity of the sun

The interaction between dust and gas with the interstellar radiation is critical to determine the physical state of the ISM. The chemical and ionization state depends on the rates of photoionization and photodissociation, the heating depends on the interaction with the photons of the electromagnetic field. Specifically, interstellar radiation in the proximity of the Sun is dominated by 6 components:

- Galactic synchrotron radiation from relativistic electrons.
- The cosmic microwave background radiation.
- Far-infrared (FIR) and infrared (IR) emission from dust grains heated by starlight.
- Emission from $\sim 10^4[K]$ plasma -free-free, free-bound, and bound-bound transitions.
- Starlight-photons from stellar photospheres.
- X-ray emission from hot (10^5 to $10^8[K]$) plasma.

1.5 Origin of Fine-Structure lines

Driven by nucleosynthesis in stars, the three most abundant elements in the Universe after hydrogen and helium are oxygen, carbon, and nitrogen. The emission or absorption lines, represents electrons moving from one energy level to another, about an atomic nucleus. Such

Table 1.2: A denotes the total orbital angular momentum of the electrons in an atom. This table shows the different values and names that the angular momentum of an electron can take.

Notation	value
S	0
P	1
D	2
F	3

transitions involve significant changes of energy, ΔE . These energy levels are described by the principal quantum number, n , which indicates the distance of the energy level from the nucleus. In fact, the main quantum number refers to a probability of finding the electron in a certain energy, however the distance interpretation gives a good notion. The other quantum numbers are l , m and s . For one electron, the orbital angular momentum, l_i , and spin angular momentum, s_i , are also quantized. Summing over all electrons within the atom, are obtained the total spin and angular momentum quantum numbers, $S \equiv \sum s_i$ and $L \equiv \sum l_i$. The interaction of S and L split the energy shell in subshells. These subshells are relatively low-energy and are the source of THz fine-structure lines.

These transitions are denoted by $^{2S+1}A_J$, where the superscript $2S + 1$ is equivalent to the total number of levels into which the spin term is split, A denotes the total orbital angular momentum given by table 1.2

J denotes the magnitude of the vector sum of L and S: $J \equiv L + S$ (See figure 1.5), and each J level has a degeneracy given by $m_J = 2J + 1$, since these transitions do not result in a change of electronic configuration, they are classified as forbidden lines, meaning they radiate through less efficient magnetic dipole transitions, not through electric dipole transitions. Compared to the probability of an electric dipole transition, magnetic dipole transitions are metastable, its transition times are measured in days.

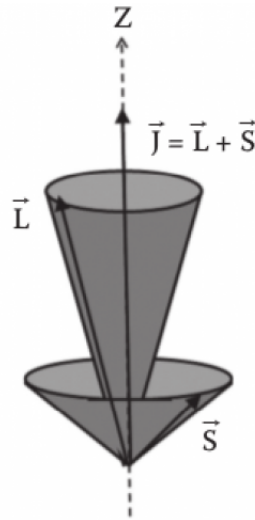


Figure 1.5: L and S generate sub-shells, which are seen as atomic fine-structure lines. And J is the total angular momentum operator.

1.6 Molecular Line Spectra

Symmetric molecules have no permanent electric dipole moment and these are called "apolar". A molecule is called "polar" if it has nonzero permanent electric dipole moment (because have significantly asymmetric charge distributions). Polar molecules radiate at their rotation frequency ω . The angular momentum is quantized, to see that, is used the De Broglie wavelengths.

$$\lambda = \frac{h}{p} = \frac{h}{m_e v}$$

In the last equation p is the electron's momentum and v is its speed. Approximately, orbits whose circumferences are equal to an integer number n of Broglie wavelengths corresponding to orbits permitted. Therefore

$$2\pi a_n = n\lambda = \frac{nh}{m_e v}$$

where a_n is the Bohr's radio. In this case is equal to

$$a_n = \frac{nh}{2\pi m_e v} \quad (1.6.1)$$

$$= \frac{n\hbar}{m_e v} \quad (1.6.2)$$

The orbital angular momentum is $|\vec{L}| = |\vec{r} \times \vec{p}| = |rpsin(\theta)|$. If \vec{r} and \vec{p} are perpendicular, the module of \vec{L} is $L = rmv = a_n m_e v$. The module of angular momentum can be written as

$$L = n\hbar \quad (1.6.3)$$

In the case of a diatomic molecule with masses m_A and m_B separated by a distance $r_e = r_A + r_B$, r_A and r_B are the distance from the center of the mass. The masses and distances must obey.

$$r_A m_A = r_B m_B \quad (1.6.4)$$

If the molecule is rotating about its center of mass, the angular momentum can be written as

$$\vec{L} = I\vec{\omega} \quad (1.6.5)$$

where $I = m_A r_A^2 + m_B r_B^2$ is the moment of inertia and ω is the angular velocity of the rotation. Therefore

$$\vec{L} = \left(\frac{m_A m_B}{m_A + m_B} \right) r_e^2 \vec{\omega} \quad (1.6.6)$$

$$\vec{L} = m r_e^2 \vec{\omega} \quad (1.6.7)$$

Where m is the reduced mass of the molecule. The rotational kinetic energy of a rotating system is

$$E_{rot} = \frac{I\omega^2}{2} = \frac{L^2}{2I} \quad (1.6.8)$$

Using the eigenvalues of the Schrödinger equation, the kinetic energy is

$$E_{rot} = \frac{J(J+1)\hbar^2}{2I} \quad (1.6.9)$$

And the changes in rotational energy are also quantized, by $\Delta J = \pm 1$. The frequency emitted by a transition is

$$\nu = \frac{\Delta E_{rot}}{h} \quad (1.6.10)$$

The electric dipole moment \vec{d} of a charge distribution $\rho(\vec{x})$ is

$$\vec{d} \equiv \int \rho(\vec{x}) \vec{x} dx \quad (1.6.11)$$

If there are only two point charges $+q$ and $-q$ separated by r_e on some direction x , the electric dipole moment is $|d| = q r_e$. For a molecule rotating with angular velocity ω , the projection of the dipole moment perpendicular to the line of sight varies with time as $q r_e \exp(-i\omega t)$. For each charge the energy is

$$E_{\perp} = \frac{q a \sin(\theta)}{r c^2} \quad (1.6.12)$$

$$= \frac{q(\omega^2 r_A + \omega^2 r_B) \sin(\theta)}{r c^2} \exp(-i\omega t) \quad (1.6.13)$$

Where a is the module of acceleration, θ is the angle between the acceleration vector and the line from the charge to the observer and c is the speed of light. The instantaneous power emitted is

$$P = \frac{2q^2}{3c^3} \omega^4 |r_3 \exp(-i\omega t)|^2 \quad (1.6.14)$$

The time-averaged power is

$$\langle P \rangle = \frac{2q^2}{3c^3} (2\pi\nu)^4 \frac{r_e^2}{2} \quad (1.6.15)$$

$$= \frac{64\pi^4}{3c^3} \nu^4 \left(\frac{qr_e}{2}\right)^2 \quad (1.6.16)$$

$$= \frac{64\pi^4}{3c^3} \nu^4 |\mu|^2 \quad (1.6.17)$$

Where $|\mu|^2 \equiv \left(\frac{qr_e}{2}\right)^2$ is the mean electric dipole moment, and is related with the spontaneous emission coefficient as

$$A_{ul} = \frac{|P|}{h\nu_{ul}} \quad (1.6.18)$$

$$= \frac{64\pi^4}{3hc^3} \nu_{ul}^3 |\mu_{ul}|^2 \quad (1.6.19)$$

One of the most abundant molecules in the universe is CO, this molecule can excite its angular momentum, as explained in this section, mainly due to shocks with molecular gas (H₂). If the density of the medium is very high, the molecule can excite very high transitions. Some transitions and its frequencies are shown in figure 1.6

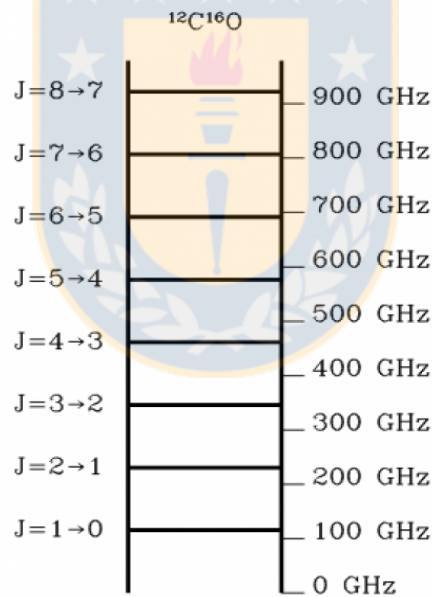


Figure 1.6: Transitions of molecule of CO. CO(1-0) is the first excitation of this molecule and emits at the lowest frequency compared to the other transitions. When the density of the medium increases, the molecule can rotate with greater energy exiting its operator angular momentum to higher values. To de-excite emits radiation, this radiation has the frequencies shown in the figure (if they are not affected by redshift).

Chapter 2

Theoretical framework

In this chapter we describe the essential topics of this thesis. In this part, the contents are very specific and are necessary to justify the research topic. First, AME is described and how can be produced. To finish with a lot of Interstellar mediums that have the same phenomenon.

2.1 Theoretical Basis

2.1.1 AME

Dust grains can be bombarded by FUV, and when the dust excite its angular momentum operator, spontaneously emits radiation to de-excite itself, and this spontaneous radiation is the best candidate for AME, and this process in the literature is often associated to spinning dust. It is easy to make the analogy between the angular momentum and orbitals of an atom, regarding the excitation.

AME, anomalous microwave emission, was discovered in 1990 studying CMB. Was an excess in detected power between 10-60 [GHz] and the usual mechanisms of emission couldn't explain this excess. AME was found in different molecular clouds in our galaxy, even in extragalactic sources. The best candidate to be responsible for this excess emission is the spinning dust, which was predicted in 1950 (Dickinson et al. (2013)).

The theory predicts a peak between 10-100[GHz]. This peak covers a very long range of frequencies and it is very dependent on the size of the dust grains. There is still debate about the real nature of AME.

This emission is very correlated with the dust in the ISM, and we can see an excess of emission with respect to the predicted thermal emission and dust emission at these frequencies There are a few handfuls of detections, Perseus and Oph molecular clouds, LDN 1622, LDN 1621, LDN 1111, and a variety of HII regions. Additionally, the first detection of AME in a star forming region in the external galaxy NGC6946, was reported.

AME occurs in the frequency range 10 -100 [GHz] and is highly correlated with the mid-infrared dust emission (Draine and Lazarian (1998)). This correlation led to Draine and Lazarian to postulate their model of spinning dust emission, here the excess is produced by the very smallest dust grains (very small grains; VSGs or Polycyclic Aromatic Hydrocarbons; PAHs), characterized

by an electric dipole moment, rotating rapidly, resulting in the production of electric dipole radiation. The model is very well defined to 20-30 [GHz].

Adaptations to the model by Ali-Haimoud, Hirata and Dickinson, 2009; Hoang et al., 2010; Ysard and Verstraete, 2010; Hoang et al., 2011; Silsbee et al, 2011 (Y. Ali-Haimoud et al., 2009; Hoang et al., 2010; Ysard & Verstraete, 2010; Hoang et al., 2011; Silsbee et al., 2011); incorporate a variety of grain rotational excitation and damping processes: collisions with neutral and ionized gas particles, plasma drag (the interaction between the electric field of ions and the electric dipole moment of the dust grains), absorption and emission of a photon, the photoelectric effect, microwave emission and the formation of H_2 on the grain surface.

Adaptations to the model by Hoang et al, 2010 and 2011 (Hoang et al., 2010; Silsbee et al., 2011); Silsbee et al 2011 (Hoang et al., 2011), incorporate dust grain that are not only spinning about their axis of the greatest inertia and dust grains of irregular shape.

2.1.1.1 Definition of AME emissivity

Given the strong association between the AME and the dust grains in the ISM, the AME emissivity is usually defined as the ratio between the antenna temperature of the AME at wavelengths of 1 [cm] and the surface brightness of the thermal dust emission at 100 [μm]. This ratio is calculated as a cross-correlation coefficient over a variety of individual regions in which AME has been detected (see table 2.1 (Tibbs et al., 2012)).

Don't forget that antenna temperature is measured in K and the surface brightness (in radio astronomy) is measured in $\frac{W}{m^2 Hz sr^{-1}}$ and is very useful and used $1[Jy] = 10^{-26}[W/m^2 Hz]$.

In table 2.1 there are listed AME emissivities defined relative to the 100[μm] emission, it is possible to identify the observed range of values of the AME emissivity, from 3 to 25 $\mu K(MJy sr^{-1})^{-1}$, with a typical value of $10\mu K(MJy sr^{-1})^{-1}$. Using this value, we have that

$$\frac{T_{an}}{B_{source}} = \frac{10 \mu K}{1 \frac{MJy}{sr}} \quad (2.1.1)$$

$$= \frac{10^{-11} K}{1 \frac{Jy}{sr}} \quad (2.1.2)$$

$$(2.1.3)$$

In term of flux density we have.

$$S = \frac{2k \times 10^{-5} (3 \times 10^{10})^2}{(3 \times 10^8)^2} \quad (2.1.4)$$

$$= \frac{2,484 \times 10^{-7} [(J/K) Hz^2 K]}{9 \times 10^{16} [m^2/s^2]} \quad (2.1.5)$$

$$= 2,76 \times 10^{-24} [J/m^2] \quad (2.1.6)$$

$$= 276[Jy] \quad (2.1.7)$$

Table 2.1: Sample of AME emissivity values, for AME detections in a variety of different environments computed relative at emission at 100 [μm].

Source	AME Emissivity ($\mu K (MJy sr^{-1})^{-1}$)	Reference
Hii Regions		
6 southern HII regions	3.3 ± 1.7	Dickinson et al. (2007)
9 northern HII regions	3.9 ± 0.8	Todorović et al. (2010)
Pleiades	2.01 ± 0.09	Génova-Santos et al. (2011)
RCW49	13.6 ± 4.2	Dickinson et al. (2007)
RCW175	14.2 ± 2.7	Tibbs et al. (2012a)
High Latitudes		
15 regions <i>WMAP</i>	11.2 ± 1.5	Davies et al. (2006)
All-sky <i>WMAP</i>	10.9 ± 1.1	Davies et al. (2006)
Molecular Clouds		
Perseus	15.7 ± 0.3	Watson et al. (2005)
Perseus A1	2.8 ± 0.7	Tibbs et al. (2010)
Perseus A2	16.4 ± 4.1	Tibbs et al. (2010)
Perseus A3	12.8 ± 6.1	Tibbs et al. (2010)
Perseus B	13.2 ± 3.6	Tibbs et al. (2010)
Perseus C	13.0 ± 3.2	Tibbs et al. (2010)
Dark Clouds		
LDN1621	18.1 ± 4.4	Dickinson et al. (2010)
LDN1622	21.3 ± 0.6	Casassus et al. (2006)

The flux density with $10\mu\text{K}$ is approximately $300[\text{Jy}]$, so

$$\frac{S_{an}}{S_{source}} = \frac{300[\text{Jy}]}{1[\text{MJy}]} \quad (2.1.8)$$

$$= \frac{300[\text{Jy}]}{10^6[\text{Jy}]} \quad (2.1.9)$$

$$= 3 \times 10^{-4} \quad (2.1.10)$$

Here we see that, $1[\text{Jy}]$ of AME at $1[\text{cm}]$ for every $3000[\text{Jy}]$ at $100[\mu\text{m}]$. Observation at far-IR and sub-millimeter wavelengths ((e.g. Reach et al., 1995; Boulanger et al., 1996)) show that the spectrum of the dust emission is well represented by a modified black body function of the form, see the figure 2.1 (Tibbs et al., 2012)

$$S_\nu \propto \frac{2h\nu^{3+\beta}}{c^2} \frac{1}{\exp(h\nu/kT_{dust}) - 1} \quad (2.1.11)$$

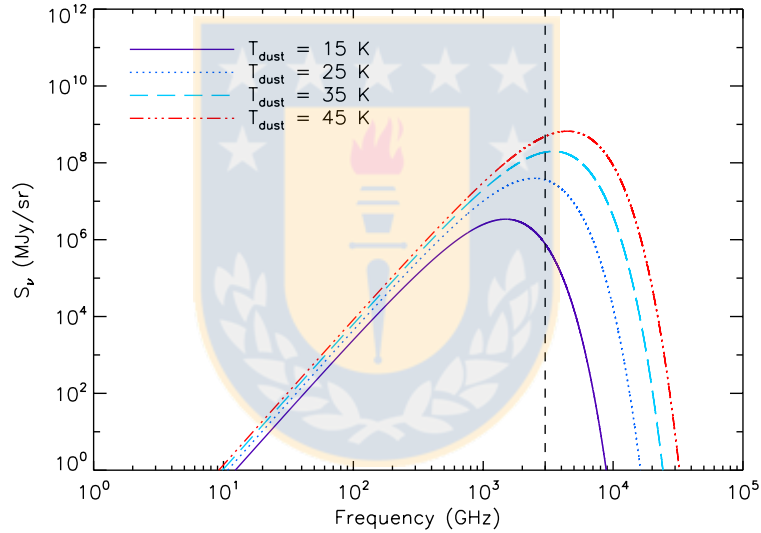


Figure 2.1: The grey body spectrum representing the thermal dust emission for a range of dust temperatures from 15 to 45 K with a fixed dust emissivity spectral index of 1.8. The $100[\mu\text{m}]$ emission (vertical dashed line) increases with increasing dust temperature.

This spectrum is produced by a balance between absorption (of big dust grains absorbing ultra-violet photons) and emission (the dust re-radiating that ultra-violet photons thermally), this keeps the big grains in thermal equilibrium. AME emissivity can be calculated relative to the hydrogen column density, N_H , this has several advantages; first because the AME emissivity is more comparable with the theoretical values as the current spinning dust theories compute an emissivity in units $\text{Jysr}^{-1}\text{cm}^2$ per H atom. The term Jysr^{-1} is given by the surface brightness of

Table 2.2: AME emissivity values computed relative to the hydrogen column density.

Source	N_H (10^{22} H cm^{-2})	AME Emissivity (10^{-18} Jy sr^{-1} cm^2/H)	Reference
Perseus A1	0.82 ± 0.19	2.2 ± 0.5	(Tibbs et al., 2012)
Perseus A2	1.19 ± 0.27	2.7 ± 0.6	(Tibbs et al., 2012)
Perseus A3	1.28 ± 0.29	1.2 ± 0.3	(Tibbs et al., 2012)
Perseus B	0.79 ± 0.18	3.4 ± 0.8	(Tibbs et al., 2012)
Perseus C	0.74 ± 0.17	3.6 ± 0.8	(Tibbs et al., 2012)
Cirrus	0.15 ± 0.07	4.6 ± 2.0	Leitch et al. (1997)
ζ Oph	0.22 ± 0.02	4.1 ± 0.6	Vidal et al. (2011)
LDN1780	0.45 ± 0.04	3.5 ± 0.4	Vidal et al. (2011)
LDN1622	1.50 ± 0.15	2.0 ± 0.2	Casassus et al. (2006)
ρ Oph	5.00 ± 0.50	3.2 ± 0.5	Casassus et al. (2008)
M78	22.80 ± 0.23	0.9 ± 0.1	Castellanos et al. (2011)

AME at 1 $[cm]$, and cm^2 is given by the column density. Using N_H also mitigates the effects of dust temperature. See the table 2.2 (Tibbs et al., 2012)

Would be very useful use N_{dust} , but is more difficult to estimate than N_H . N_H may be computed by fitting the far-IR SED with a dust model which incorporates the physical properties of the dust grains. To finish this section, in the figure 2.2 (Battistelli et al., 2012) different models of AME are showed.

2.1.1.2 Other possibilities of AME

- According to (Bennett et al. , 2003), AME is produced by hot ferromagnetic grains, but observations have placed limits of a few percent on the fractional polarization toward AME targets.
- There are other alternative explanation of AME based on flat-spectrum synchrotron emission associated to star-forming regions, but this idea is in disagreement with ARCADE data and with results from (A. De Oliveira-Costa et al. , 2010), (S. Fernández-Cerezo et al. , 2006), (S. R. Hildebrandt et al., 2007) and (Ysard & Verstraete, 2010).

2.1.2 Dust grain

The interstellar dust seems perfect to describe the AME (due to its rotation). But there are different types of dust grains, with different compositions, size and shape.

Dust grain can be bombarded by FUV and it can start to spin, and this component is often called "spinning dust". The best candidate to produces AME is by small grains such as PAHs.

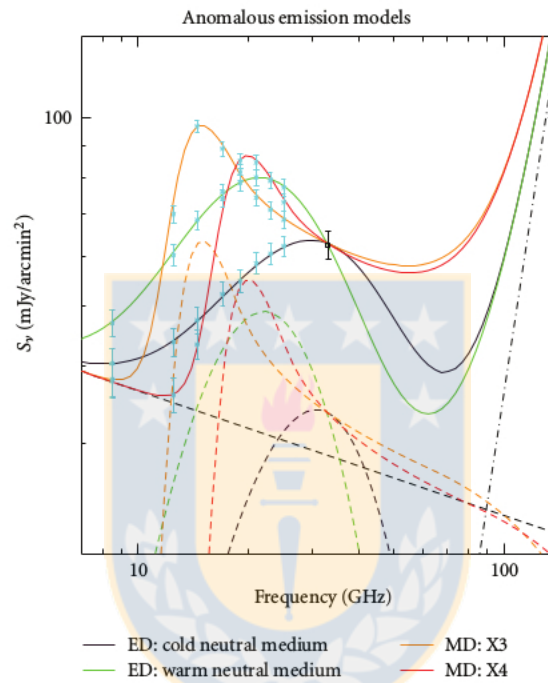


Figure 2.2: The combination of free-free emission (dashed line) plus thermal emission (dot-dashed line) is inconsistent with the 33[GHz] signal shown here. It is necessary to consider an additional contribution (spinning dust). This is provided by different models of AME for electric dipole (ED (Draine and Lazarian, 1998)) and magnetic dipole (MD (Draine and Lazarian, 1990))

2.1.2.1 The original DL98 Model

Given the great diversity of dust grains, we need to have a model that allows to have certain assumptions and approximations that emulate and represent the state of the dust grains.

The DL98 model explains how AME is produced by small grains. In this model the smallest PAH particles are expected to be planar for $a < a_2$ and spherical for $a > a_2$ with $a_2 = 6[\text{\AA}]$, where the size a is defined as the radius of an equivalent sphere of the same mass. PAHs usually have electric dipole moment ν arising from asymmetric polar molecules. The angular momentum J ⁵ (~ 70) (Draine and Lazarian, 1998) is parallel to a_1 (symmetry axis), and J is isotropically oriented in space. To fixed, J the spinning grain emits electric dipole radiation at a unique frequency, $\nu = \frac{\omega}{2\pi}$. The grain collides with neutral atoms and ions, and emits electric dipole radiation, in this process the angular velocity randomly fluctuates and its distribution can be approximated as the Maxwellian distribution function $f_{M_w}(\omega)$. And the total emissivity per H atom of the electric dipole radiation from spinning dust at frequency ν is given by equation 2.1.12 (Hoang and Lazarian, 2012)

$$\frac{j_\nu}{n_H} = \frac{1}{4\pi} \frac{1}{n_H} \int_{a_{min}}^{a_{max}} da \frac{dn}{da} 4\pi\omega^2 f_{M_w}(\omega) 2\pi \left(\frac{2\mu_\perp^2 \omega^4}{3c^3} \right) \quad (2.1.12)$$

n_H is the density per H atom, μ_\perp is the electric dipole moment perpendicular to the rotation axis, $\frac{dn}{da}$ is the grain size distribution.

The instantaneous power radiated is given by

$$P(t) = \frac{2}{3c^3} \dot{\mu}^2 \quad (2.1.13)$$

Averaging the power radiative over many cycles (Yacine, 2013), is obtained the following expression

$$\langle P \rangle = \frac{2}{3c^3} \langle \dot{\mu}^2 \rangle \quad (2.1.14)$$

$$\langle P \rangle = \int d\nu \frac{2}{3c^3} (2\pi\nu)^4 \sum_i S_{\mu_i}(\nu) \quad (2.1.15)$$

$S_{\mu_i}(\nu)$ is the power spectrum of the i th Cartesian component of μ . The power radiated per unit frequency is

$$\frac{dP}{d\nu}(\nu|L, \bar{\omega}) = \frac{2}{3c^3} (2\pi\nu)^4 \sum_i S_{\mu_i}(\nu) \quad (2.1.16)$$

where $\bar{\omega}$ is a set of angles between grain axes and dipole moment with respect to L . The most simple case is a freely rotating spherical grain, with angular velocity given by $\vec{\omega}_0 = \frac{\vec{L}}{I}$, (I is the moment of inertia). The power spectra is given by $S_{\mu_z} = 0$ and $S_{\mu_x} = S_{\mu_y} = \frac{1}{2} \mu_\perp^2 \delta(\nu - \frac{L}{2\pi I})$.

The calculation for a triaxial grain is not analytical and the spectral power is obtained numerically.

The Fokker-Planck (FP) (Yacine, 2013) equation describes the rotational excitation of a spherical grain if the discrete nature of impulses from single-ion collisions can be neglected, and was necessary include this kind of description of grain rotation, therefore this equation include new considerations: (Silsbee et al., 2011)

⁵ Actually the angular moment is given by L and $J = \frac{L}{\hbar}$, but both describe the same physics

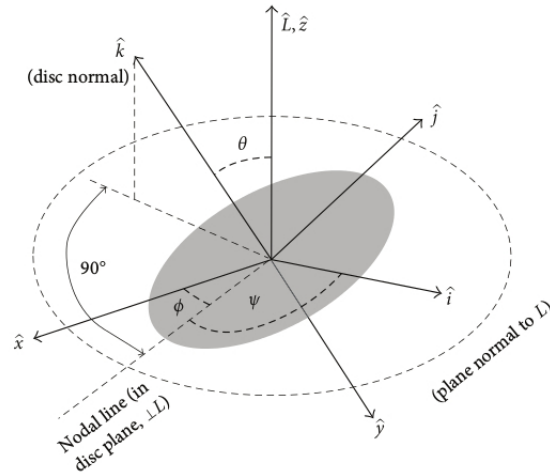


Figure 2.3: This figure show the angular momentum plane and principle axis plane, using Euler angles we can describe an axisymmetric grain. (Hoang et al., 2010, 2011).

- a_1 is not perfectly aligned with J , due to internal thermal fluctuations.
- The Fourier transform can be used to obtain the power spectrum of a freely spinning dust.
- $f_{M_w}(\omega)$, J and ω can be obtained using the Langevin equation (LE) (Hoang and Lazarian, 2012).
- Infrequent collisions of single ions are treated as Poisson-distributed events.
- The wobbling disk-like grain has anisotropic rotational damping and excitation.
- $I_1 \geq I_2 \geq I_3$ are the principal moments of a very small grain triaxial ellipsoid (irregular).
- The orientation of μ can be changed due to internal thermal fluctuations.
- There are considerable effects of compressible turbulence on the rotation of a grain.

For axisymmetric grains $I_3 > I_2 = I_1$. To describe the misalignment between L and the principal axis, the Euler angles are used, see Figure 2.3 . So

$$\theta = \text{constant} \quad (2.1.17)$$

$$\dot{\phi} = \frac{L}{I_1} \quad (2.1.18)$$

$$\dot{\psi} = -\left(\frac{L}{I_1} - \frac{L}{I_3}\right)\cos(\theta) \quad (2.1.19)$$

From (Yacine, 2013) electromagnetic radiation is now emitted at the frequencies $\frac{\dot{\phi}}{2\pi}$, $\frac{|\dot{\psi}|}{2\pi}$, $\frac{\dot{\phi} \pm \dot{\psi}}{2\pi}$:

$$\frac{dP}{d\nu} = \frac{2\mu_{\parallel}^2}{3c^3} \dot{\phi}^4 \sin^2(\theta) \delta\left(\nu - \frac{\dot{\phi}}{2\pi}\right) + \frac{\mu_{\perp}^2}{3c^3} \dot{\psi}^4 \sin^2(\theta) \delta\left(\nu - \frac{|\dot{\psi}|}{2\pi}\right) + \sum_{\pm} \frac{\mu_{\perp}^2}{6c^3} (\dot{\phi} \pm \dot{\psi})^4 (1 \pm \cos(\theta))^2 \delta\left(\nu - \frac{(\dot{\phi} \pm \dot{\psi})}{2\pi}\right) \quad (2.1.20)$$

With these considerations, the amplitude of $\ddot{\mu}_x$ at the frequency ν_k , is defined as

$$\ddot{\mu}(x, k) = \int_{-\infty}^{+\infty} \ddot{\mu}_x(t) \exp(-i2\pi\nu_k t) dt \quad (2.1.21)$$

Where k denotes the frequency mode. The emission power at the positive frequency ν_k is given by

$$P_{ed,k}(J, q) = \frac{4}{3c^3} (\ddot{\mu}_{x,k}^2 + \ddot{\mu}_{z,k}^2 + \ddot{\mu}_{y,k}^2) \quad (2.1.22)$$

q is important to describe the torque-free motion of an irregular grain having a rotational energy E_{rot} . In this case, the conserved quantities are taken, including the angular momentum J and a dimensionless parameter that characterizes the deviation of the grain rotational energy from its minimum value

$$q = \frac{2I_3 E_{rot}}{J^2}$$

The total emission power from all frequency modes for a given J and q then becomes

$$P_{ed}(J, q) = \sum_k P_{ed,k}(J, q) \equiv \frac{1}{T} \int_0^T dt \left(\frac{2}{3c^3} \ddot{\mu}^2 \right) \quad (2.1.23)$$

2.2 State of the art

2.2.1 Objects of the interstellar medium

AME is usually detected in regions associated to star formation. These regions are Molecular clouds, Warm ionized medium, Reflection Nebulae, Photodissociation region and Dark clouds.

2.2.1.1 Molecular clouds

Is an interstellar cloud, whose density and temperature are enough to form molecules, obviously H_2 is the most common molecule. Is necessary to note that Molecular clouds, Warm ionized medium, Reflection Nebulae, Photodissociation region and Dark clouds are a set of molecules (many molecules and atoms interacting) and in this way molecular cloud is a generic name to the rest of the regions.

Perseus is a very well known molecular cloud which AME was detected. Planck telescope confirmed its excess to 17.1σ (Encrenaz, 1974). It was the first cloud that polarization was measured with a detection of 3% fractional polarization.

Other detection was found in ρ Ophiuchi (Watson et al., 2005; Kulesa et al., 2005; Young et al., 2006) in the Gould Belt. It is a region with a high degree of photoionization towards its periphery due to UV flux from its hottest young stars.

Planck satellite detected an excess of microwave emission (AME) in ρ -Ophiuchus at a significance of 8.4σ (Watson et al., 2005). The last three detections show an excess in the microwave spectrum, however, were produced by different components of spinning dust in different environmental conditions. Ideally AME is better identified using telescopes with large-scale angular ($\sim 20[\text{arcmin}]$).

2.2.1.2 Warm ionized medium

This kind of regions is characteristic in pulsars. It shows H_α in its emission lines. The typical values of temperature and density of warm ionized medium (WIM), cold neutral medium (CNM) and warm neutral medium (WNM) are shown in table 2.3.

Table 2.3: Typical values of density and temperature for WIM, CNM and WNM

Medium	n_H [cm^{-3}]	Temperature [K]
WIM	0.3	$10^3 - 10^4$
WNM	0.3	$10^3 - 10^4$
CNM	30	100

AME have been detected in HII regions, but is important consider some situations. A sample of six HII regions was observed in the southern hemisphere (Dickinson et al., 2007) and they showed a possible small excess correlated with IRAS 100[μm] data with an average emissivity of $3.3 \pm 1.7[\mu\text{m}(\text{MJysr}^{-1})^{-1}]$ at 31[GHz] over the full sample and a 95% confidence limit of $< 6.1[\mu\text{m}(\text{MJysr}^{-1})^{-1}]$. The most significant detection was towards RCW 49 which indicated a 3.3σ excess at 31[GHz]. But in the other hand a sample of 16 HII regions in the Northern hemisphere (Scaife et al., 2008) showed no statistically significant excess.

There are important differences between these observations

- Were observed in not exactly the same frequency.
- Were observed in different range of angular scales. The sample of southern HII region was observed with an instrument that had sensitivity to marginally larger angular scales than the northern sample.
- In general the northern sample has less associated diffuse emission relative to the resolution of the telescope.

With the results of these observations one can think that AME can be present on larger scales free-free emission or AME may be a consequence of an inverse relationship between VSG abundance and density resulting in a lower spinning dust emissivity. Another possibility for the identification of AME from HII can be by the presence of Ultra -or hypercompact HII regions because have a significant contamination from dense plasma (Scaife, 2013).

The HII region RCW 175 have the most convincing detection of AME, the excess at 31 – 33[GHz] with 8.6σ significance, this excess is shown in figure 2.4. It has three different scenarios in figure 2.4 to explain the SED of RCW 175. In (a) a simple power law radio spectrum plus a greybody thermal dust spectrum, with spectral index $\alpha = -0.00 \pm 0.003$. In (b) a model including a thermal bremsstrahlung emission component suffering from dust absorption at high frequencies. In (c) a model with a power law component and a spinning dust component. And the last is the most consistent scenario with the observations.

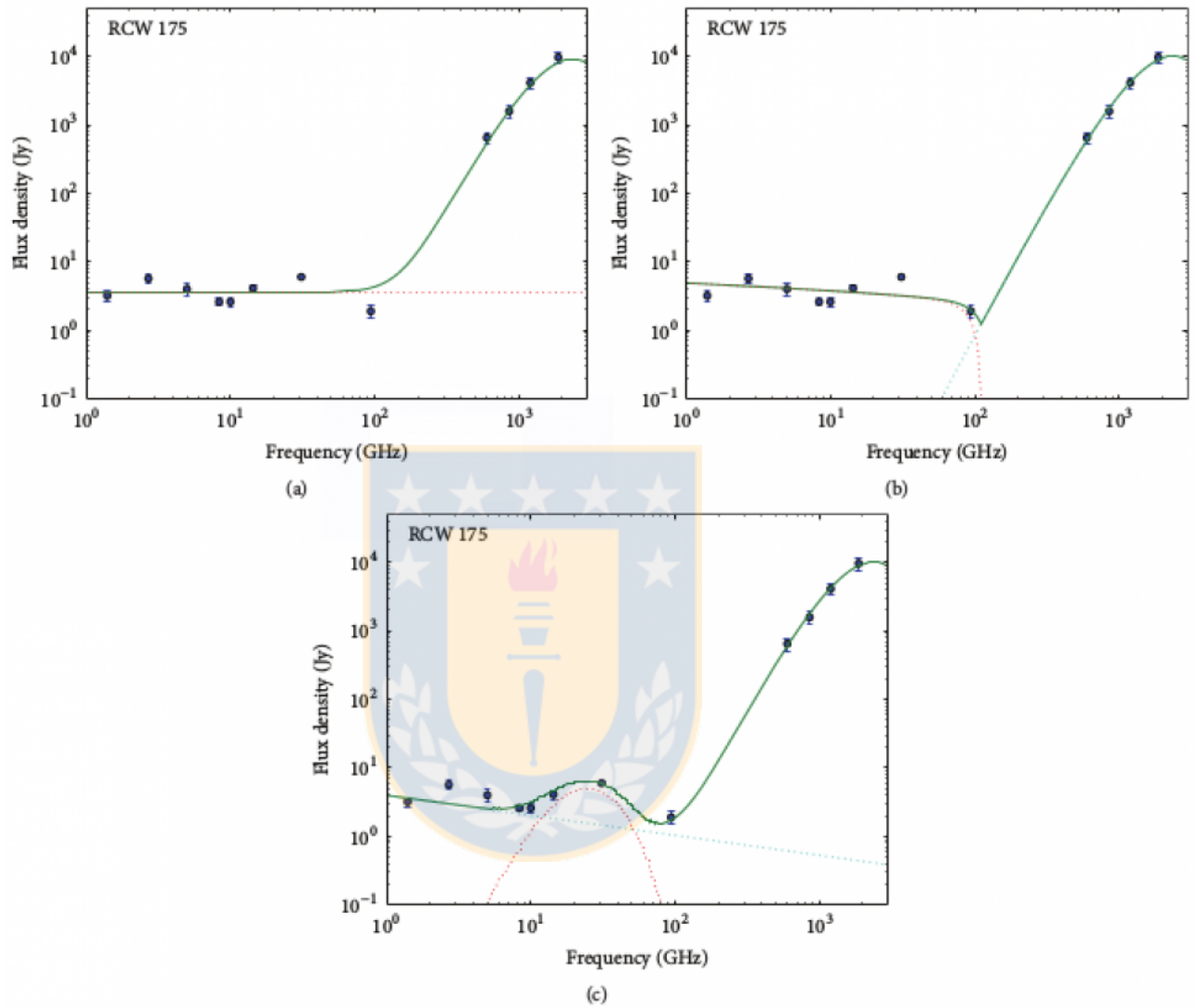


Figure 2.4: SED of RCW 175, with $\beta = 2$ and $T_d = 22.9[K]$. The data are fitting using three different scenarios. (a) Power-law radio emission plus thermal dust greybody. (b) Thermal bremsstrahlung with dust absorption plus thermal dust greybody. (c) Power-law radio emission plus spinning dust plus thermal dust greybody (Scaife, 2013)

2.2.1.3 Dark clouds

This kind of region has a high visual extinction ($A_v \approx 3[mag]$). The extinction of the light is caused by interstellar dust grains located in the coldest, densest parts of larger molecular clouds (the most important element that attenuate the light are C and S). Unlike the HII regions, in dark clouds the radio emission not expected due to its low ionization fraction. LDN 1622 have the most significant AME found in a dark cloud(see the following sections). From a sample of 14 dark clouds (Scaife, 2013), AME was identified only in two samples L675 and L111, and only three possible candidates L944, L1103 and L1246 (L944 and L1246 are proto-stellar clouds). The values of AME to L675 and L111 are 16.4 ± 1.8 and $28.5 \pm 3.3[\mu K(MJysr^{-1})^{-1}]$, respectively. This 5 dark clouds were re-observed at higher resolution at radio frequencies (Scaife, Nikolic et al., 2010) (Scaife, Green et al., 2010) to establish whether the microwave emission followed the same distribution as the dust traced by sub-mm observations. The dark cloud L675, which was assumed to be starless, hosted a compact radio source coincident with the peak of the $850[\mu m]$ sub-mm emission. And the coincidence of a compact sub-mm peak with a radio point source is strong evidence for protostellar activity (Rodriguez et al., 1993). This raised the question of whether it is possible to accurately investigate any correlation of AME with protostellar activity, but it is still an open question. In L1246 was detected a correlation with PAH (Scaife, Nikolic et al., 2010) (Scaife, Green et al., 2010) given by the observations of Spitzer band 4.

The dark clouds sample of (Scaife et al., 2009) was selected from the sub-mm survey of (Visser et al., 2001) and an inverse relationship between column density and molecular hydrogen was found. It is possible that this negative correlation represents the depletion of small grains in denser environments, see Figure 2.5, (Scaife, 2013).

2.2.1.4 Reflection Nebulae

Reflection Nebulae are regions of gas bombarded by FUV insufficient to ionize but enough to illuminate. This kind of regions are associated with massive regions of stellar formation and object pre-SP.

Reflection nebulae are not expected to emit at radio frequencies because they lack a high degree of ionization. The M78 region is part of the dark cloud L1630 within the Orion molecular cloud. It contains a number of reflection nebulae (NGC 2068, NGC 2071, NGC 2064, and NGC 2067). AME was found in NGC 2023 and L1630⁶ (both in Orion molecular cloud).

The LDN 1622 also hosts a reflection nebula (Scaife, 2013).

2.2.1.5 Photodissociation Regions

Are regions dissociated by FUV, enough to dissociate molecules like O_2 in outer layers, but insufficient to ionize the gas and insufficient to dissociate H_2 .

The first, tentative, detection of AME was made with VSA telescope (Scaife et al., 2007). This PDR was associated with the supernova remnant 3C396. The excess emission at $33[GHz]$ was significant at the 7σ level. Strong $31[GHz]$ emission from ρ -Ophiuchus W PDR was detected with CBI telescope (Casassus et al., 2008), but no data on radio emission to complement the study.

⁶ P. Andre, D. Ward-Thompson, and M. Barsony, in *Proceedings of the Protostars and Planets Conference*, p. 59.

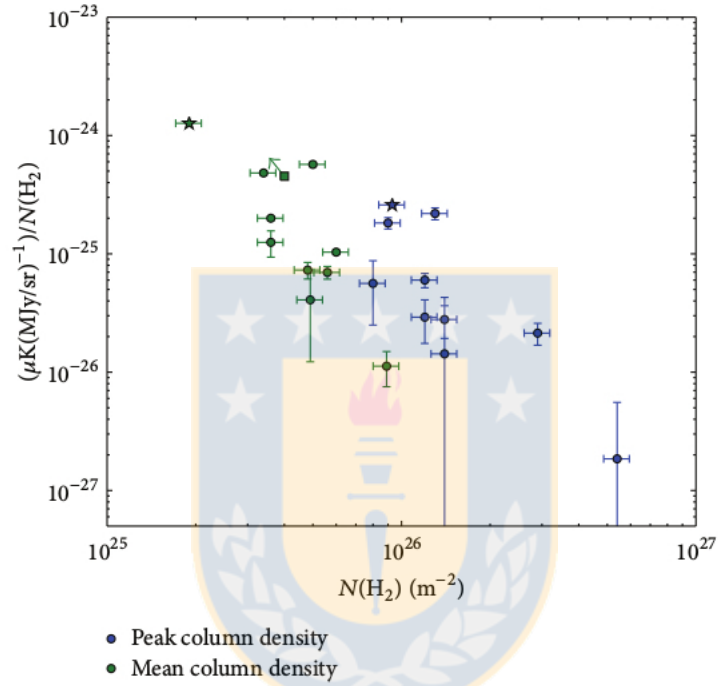


Figure 2.5: Relative emissivity of microwave emission at 100 μm FIR emission as a function of molecular hydrogen column density, $N(H_2)$, for dark clouds. Clouds from (Scaife et al., 2009) and (Scaife, Hurley-Walker et al., 2009) are shown as filled circles, LDN 1622 (Casassus et al., 2006) is shown as filled stars, and LDN 1621 (Dickinson et al., 2010) is shown as a filled square.

Chapter 3

Observations and Data reductions

3.1 Observations

In order to trace dense and cooler nuclei we observe $CO(2-1)$, $^{13}CO(2-1)$, $C^{18}O(2-1)$, $CO(3-2)$, $CO(4-3)$ and $CI[1-0]$. All those observations were taken using the technique On-The-Fly (OTF).

$CO(3-2)$ was observed with ASTE telescope (with the 1024 channel autocorrelator backend) in September 2015 (See Figure 3.2) located 4,800 meters above sea level at the Atacama Desert in Northern Chile. ASTE has a diameter of 10[m] and its beam at 350[GHz] is of 22". The observation was centered in $RA/DEC = 05 : 54 : 23 / + 01 : 46 : 54$, and the pointing was realized every 4.6" in RA. The total time of integration is of 4[h] with a mean water vapor of 0.75.

$CO(2-1)$, $^{13}CO(2-1)$ and $C^{18}O(2-1)$ was observed with CSO in February 2015 (See Figure 3.1), is housed in a compact dome at 4070 m altitude near the summit of Maunakea, Hawaii. It has a diameter of 10.4[m]. The time for each scan was 1[s], the observation was centered in $RA/DEC = 05 : 45 : 14 / + 01 : 45 : 00$ and tracking was done every 15" in RA.

The rest of the observations were taken with APEX(SHeFI) telescope in September 2017 (See Figure 3.3). APEX is located at Llano de Chajnantor, 50[Km] east of San Pedro de Atacama, Northern Chile. The time for each scan was 1[s] and 0.2[s] for CI and CO(4-3) respectively, the observation was centered in the same coordinates as COS observations and tracking was done every 4" in RA.

The data of ASTE was reduced using NOSTAR; the rest of the data was reduced using GILDAS/CLASS. Here we use the typical mechanisms to work with the data. Just from maps of CI and CO(4-3) was necessary to remove saturated pixel.

The rest frequencies of the targeted lines are listed in Table 3.1.

Table 3.1: Lines observed in this work.

Line	Transition	Rest Freq (MHz)
CO	2-1	230538
^{13}CO	2-1	220398
C^{18}O	2-1	219560
CO	3-2	345795
CO	4-3	461040
CI	$^3P_1 - ^3P_0$	492160

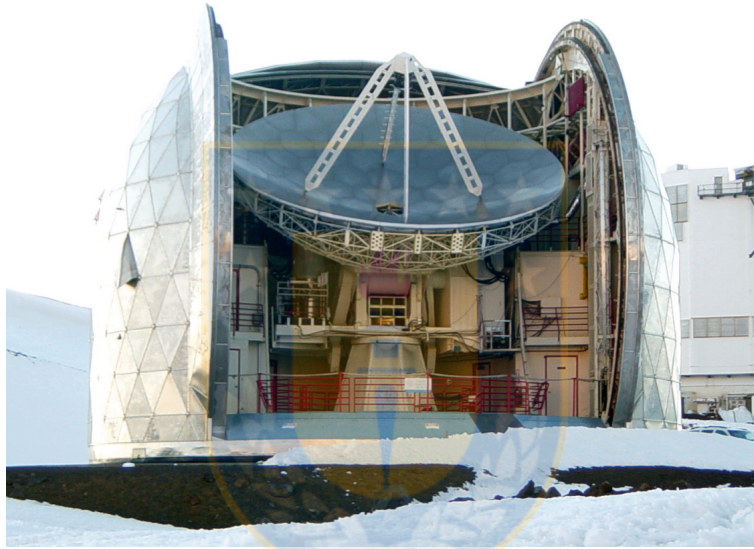


Figure 3.1: The CSO consists of a 10.4[m] diameter Leighton telescope on Mauna Kea, Hawaii. A full complement of heterodyne receivers covers the atmospheric windows from 177 to 920[GHz]. The Surface accuracy is less than $15[\mu\text{m} * r.m.s.]$, pointing accuracy if of $3[\text{arcsec} * r.m.s.]$ and its highest angular resolution is $8[\text{arcseconds}]$



Figure 3.2: ASTE is located 4,800 meters above sea level, at the Atacama Desert in Northern Chile, it observes sub-millimeter ($0.1[mm]-1[mm]$) wavelengths. Telescope diameter is $10[m]$ and Beam size at $350 [GHz]$ is $22''$.



Figure 3.3: APEX is a 12-meter diameter telescope, operating at millimeter and sub-millimeter wavelengths between infrared light and radio waves. A beam of $18''$ at $345[GHz]$ CO(3-2)

3.2 Data reductions

NOSTAR was used to work the data from ASTE (CO (3-2)). The first function used is SPLIT, because the raw data contains spectra of all the spectrometers used. Next was used the "Scaling" function to scale the data the files resulting from the split function.

At this point was necessary to subtract the baseline, with this it is sought to eliminate any own contribution of the sky or noise granted by the instrument. To do this, the functions "Baseline" and "Base" are used. The most important is to give the degree to the polynomial of adjustment and establish the range of speeds where the emission is. See Figure 3.4.

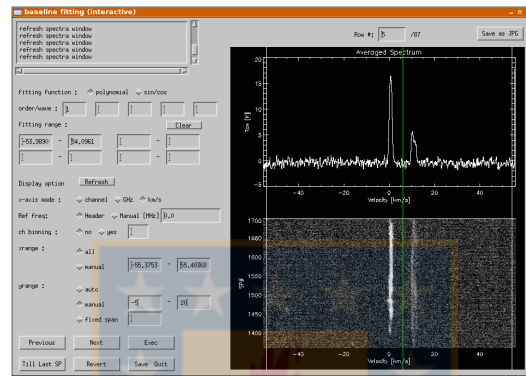


Figure 3.4: In this window, the data reduction process is started. A mainly grade 1 polynomial baseline was used. Using the cursor, the range of the base line is marked. The x-axis was left in Km / s, and the y-axis was adjusted between -5 and 20 [K] for most spectra. This function generates two new files ending in .base and .base.his. Source: Our work.

By last, "Make Map" and "Basket-Weave" were used for creates the data cube. Specifically, "Basket-Weave", combines the two images created in the previous functions, to form a data cube. It is very important that the two images that we will merge to create the data cube must have the same dimension.

From the data cube we obtained the image of LDN1622 in CO(3-2).

GILDAS/CLASS was used to reduce CSO and APEX data. This software is compatible with any linux distribution. In this case it was convenient to make a script(Appendix 4) that would reduce the data of the 5 molecular lines, CO(2-1), $^{13}\text{CO}(2-1)$, $\text{C}^{18}\text{O}(2-1)$, CI[1-0] and CO(4-3). As in NOSTAR, here we also had a data cube. From which it was necessary to indicate the speed range of interest, See Figure 3.6.

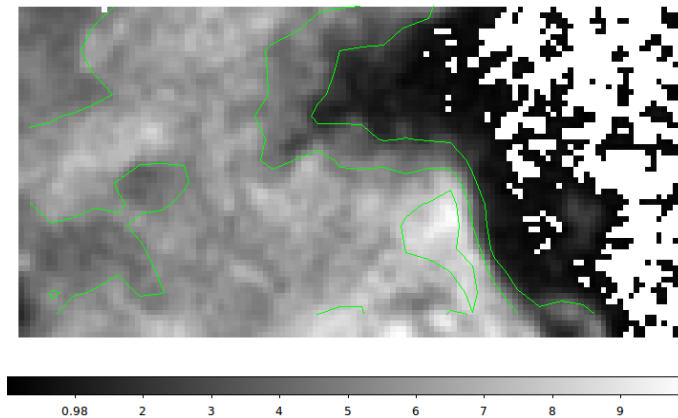


Figure 3.5: In this figure LDN 1622 is shown at the corresponding frequency of the molecular transition of CO (3-2). The contours represent temperatures of 0.05[K], 2.54[K], 5.13[K], 7.73[K] and 10.32[K]. Source: Our work.

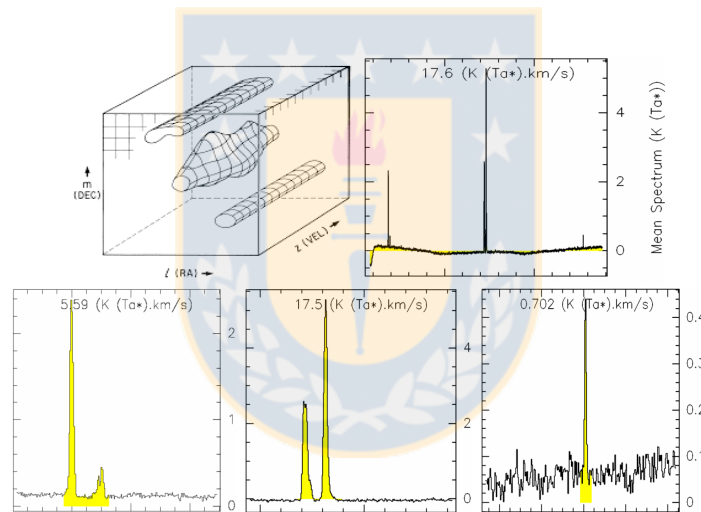


Figure 3.6: Above: On the left side there is a graphic representation of what a data cube is, each slice has spatial coordinates (RA, DEC) and represents a certain speed range. The set of all the slices is what we know as a data cube. On the right side we have the average spectrum of all the slices and all the pixels. You can see 3 broadcast peaks. Below: We zoom to the 3 peaks above and obtain from left to right graphs of temperature (K) v/s speed (km/s) of ^{13}CO , ^{12}CO and C^{18}O . To obtain the temperature graphs, you must select the desired speed ranges, as shown in the 3 graphs. Source: Our work.

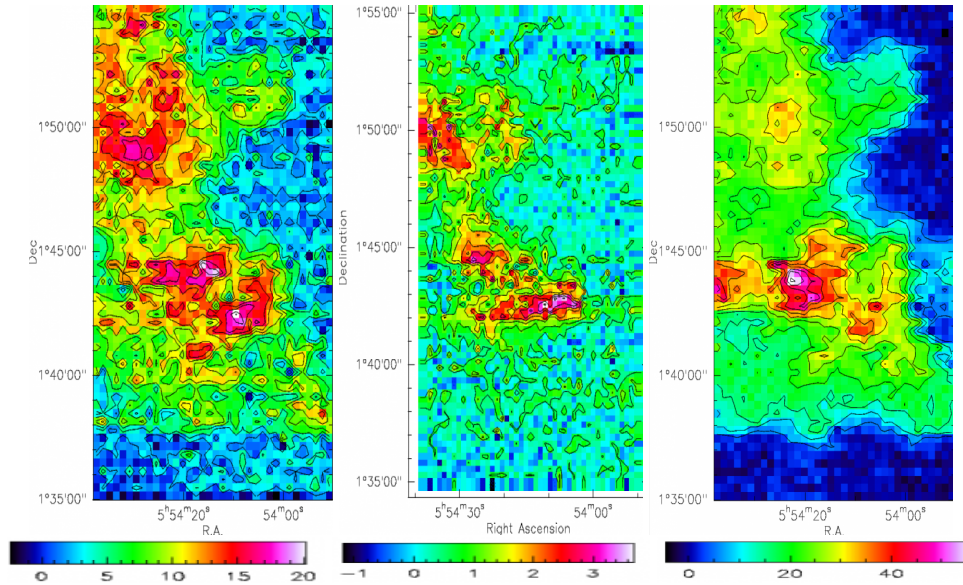


Figure 3.7: This Figure shows the speed maps of LDN1622 at the frequencies of $^{13}\text{CO}(2-1)$ (Left) $\text{C}^{18}\text{O}(2-1)$ (Middle) and $\text{CO}(2-1)$ (Right) transitions. $^{13}\text{CO}(2-1)$ thin compared to $\text{CO}(2-1)$, so with $^{13}\text{CO}(2-1)$ we can observe deeper regions. However, the densest and most agglomerated nuclei can be seen with $\text{C}^{18}\text{O}(2-1)$, between the declinations $1^{\circ}40'00''$ and $1^{\circ}45'00''$ a very dense region is appreciated as well as near the declination $1^{\circ}50'00''$ and straight elevation $5^{\text{h}}54^{\text{m}}35^{\text{s}}$. Source: Our work.

3.3 Results

In order to establish a correlation between $\text{CO}(3-2)$ and $\text{CO}(2-1)$, the contours of $\text{CO}(3-2)$ over $\text{CO}(2-1)$ are shown in Figure 3.8. Both observations are well correlated and are intended to trace cold and dense nuclei. The locations of these nuclei were found inside the cloud (as expected) and not on the periphery. For the set of stars that is near the cloud prevents the formation of these nuclei in the outer layers of the cloud, because the UV flow heats these zones.

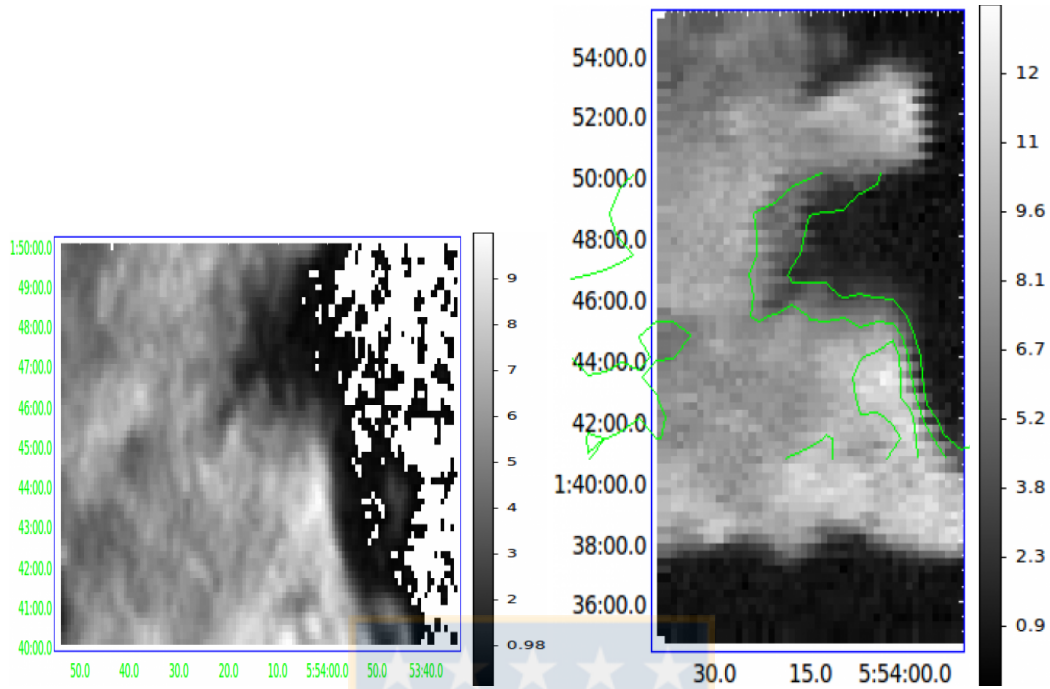


Figure 3.8: Left: Temperature map of LDN1622 at 345[GHz]. Right: Temperature map of LDN1622 at 230[GHz], the green contours come from the emission of CO(3-2), with level steps of about 2.6[K]. The images shows a good spatial correlation. Source: Our work.

With CO(2-1) and $^{13}\text{CO}(2-1)$ data, the molecular gas column density ($N(\text{H}_2)$) will be estimated. The procedure described here was taken from (Pineda et al., 2010).

The procedure will be different for regions that have CO(2-1) and $^{13}\text{CO}(2-1)$ emissions (mask 2) and for those that only have emission of CO(2-1) (mask 1).

For regions with both detections, it is necessary to extract temperature maps from the CO(2-1) and $^{13}\text{CO}(2-1)$ maps of Figure 3.7. These maps are shown in Figure 3.9.

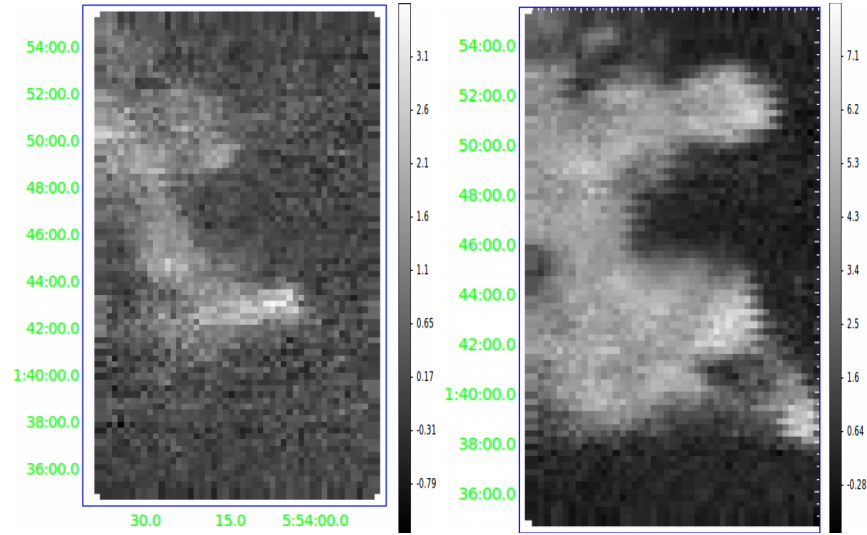


Figure 3.9: Left: Map of temperature of LDN1622 at the transitions of $C^{18}O(2-1)$. Right: Map of temperature of LDN1622, at the transition of $^{13}CO(2-1)$. $^{13}CO(2-1)$ is distributed evenly within the cloud, while $C^{18}O(2-1)$ begins to be noticed only in the interior regions. Source: Our work.

Equation 3.3.1 should be used to obtain the transition temperature of ^{13}CO at its transition (2-1)

$$T_{mb,c} = T_0 \left[\frac{1}{e^{\frac{T_0}{T_{ex}}} - 1} - \frac{1}{e^{\frac{T_0}{T_{bg}}} - 1} \right] (1 - e^{-\tau}) \quad (3.3.1)$$

Where $T_{mb,c}$ is the antenna temperature corrected for the main beam factor, which is 0.76, $T_0 = \frac{h\nu}{k}$ where h is the Planck constant, k is the Boltzmann constant, and ν is the frequency at which the molecule emits. T_{bg} is the background radiation temperature, τ is the optical depth. And T_{ex} is the excitation temperature required to clear.

To obtain T_{ex} , it is necessary to estimate the value of τ , which is approximately given by equation 3.3.2

$$\tau = \ln\left(\frac{R}{R-1}\right) \quad (3.3.2)$$

Where R is valid only for regions where there is emission in the maps of Figure 3.7 with a signal to noise greater than 3.5 sigma. However, R is the ratio (specifically, ratio of $^{12}CO/^{13}CO$) between the temperature maps of Figure 3.9.

In addition, it is necessary to calculate the column density for $^{13}CO(2-1)$, this is obtained with equation 3.3.3

$$N_U(thin) = \frac{8\pi k\nu_0^2}{hc^3 A_{UL}} \int T_{mb}(v) dv \quad (3.3.3)$$

Where A_{ul} is the Einstein A-coefficient, in this case the value of A_{ul} is $6.04 \times 10^{-1} [\frac{1}{s}]$. In the part of the integral, we use pixel by pixel the image of $^{13}CO(2-1)$ of the Figure 3.9. With this, the total

column density of the ^{13}CO molecule can be calculated. See equation 3.3.4

$$N(^{13}\text{CO}) = N_U \frac{1}{2J+1} \left[\sum_{J=0}^{\infty} (2J+1) e^{-\frac{hB_0(J+1)}{kT_{ex}}} \right] e^{-\frac{hB_0J(J+1)}{kT_{ex}}} \quad (3.3.4)$$

Where B_0 is the rotational constant of ^{13}CO given by $5.52 \times 10^{10} [\frac{1}{s}]$. It is assumed that the relationship between ^{13}CO and ^{12}CO is given by

$$N(^{12}\text{CO}) \approx 57 \times N(^{13}\text{CO})$$

In the galactic plane we can assume that the extinction is given by

$$A_v = \frac{N(^{12}\text{CO})}{1.01 \times 10^{17}} \quad (3.3.5)$$

To finally reach the relationship between extinction and molecular gas density. See equation 3.3.6

$$N(\text{H}_2) = 9.4 \times 10^{20} \times A_v \quad (3.3.6)$$

In figure 3.10 we can see the final density map, resulting from the procedure described above.

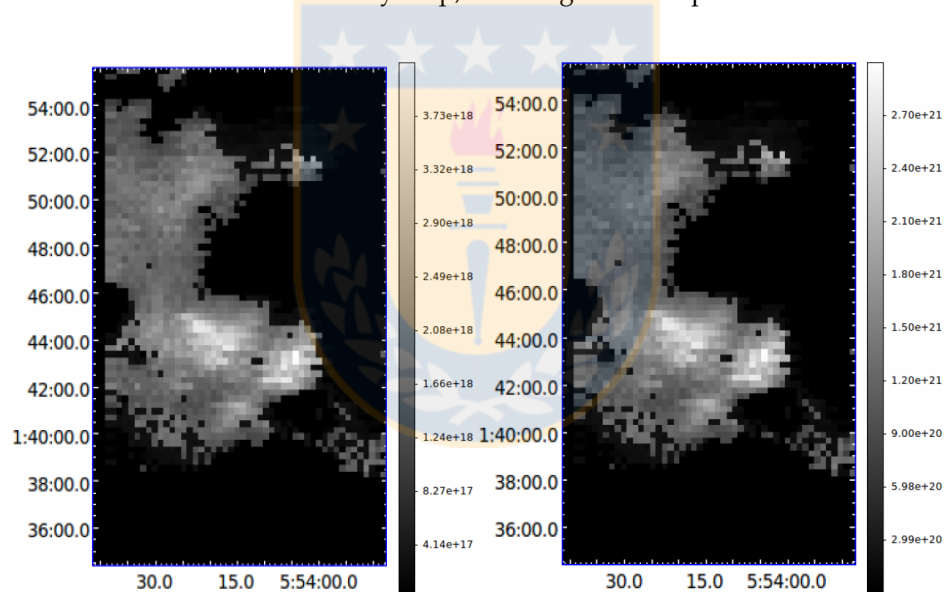


Figure 3.10: The final column density map of LDN1622 is displayed, only were considered regions where ^{13}CO and ^{12}CO were detected. Left: CO column density map. Right: H_2 column density map. Source: Our work.

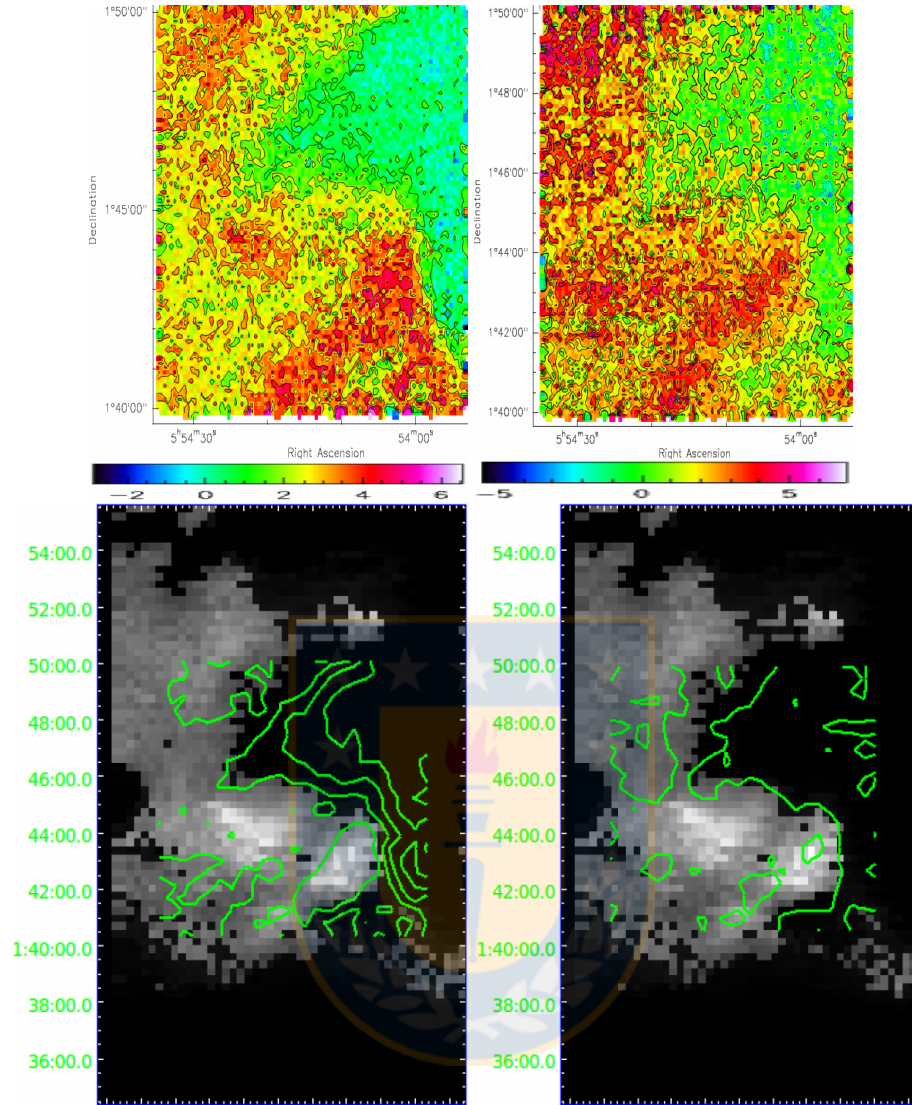


Figure 3.11: UP: Maps obtained with APEX, on the left is the CO(4-3) temperature map and on the right the CI[P₁-P₀] temperature map. DOWN: Both images correspond to the column density map of LDN1622, in the image on left the CO(4-3) contours are superimposed, in the image on the right side the CI[P₁-P₀] contours are superimposed. Both quantities are spatially correlated because the radiation dissociates the CO molecule. Therefore probable to find neutral carbon in regions bordering on CO. Source: Our work.

With data of APEX we obtain the maps shown in Figure 3.11. Since it is expected that some regions suffers of molecular dissociation, the CO will dissociate into C and O. It was expected to be able to find CI within LDN1622. See Figure 3.12.

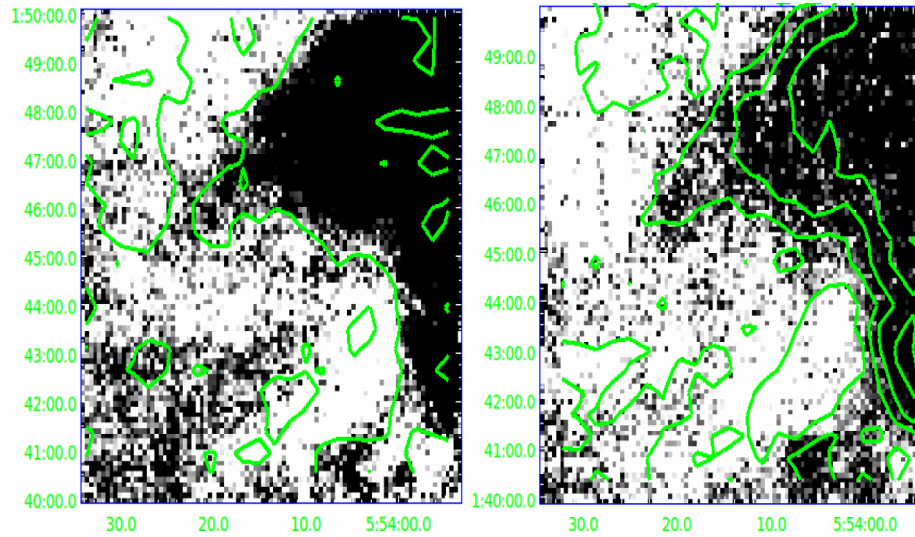


Figure 3.12: Left: Image of LDN1622 observed at $461.040[\text{GHz}]$ with contours of neutral carbon emission. Right: Image of LDN1622 observed at $492.160[\text{GHz}]$ with contours of CO(4-3). Both images show a similar spatial correlation, in particular the distribution of CI within the LDN1622 is more homogeneous than the distribution of CO(4-3). Source: Our work.

Although, with equation 3.3.5 we produced an extinction map, it is possible that this map has underestimated the extinction of very dense regions. Applying "NICER" (Near-Infrared Color Excess method Revisited) method to 2MASS near-infrared maps ldn1622 an extinction map was produced, See Figure 3.13. The NICER algorithm calculates extinction values based on the difference between the observed average near-IR color of stars within a sampling box to the stars' intrinsic average color, (Lombardi and Alves , 2001)

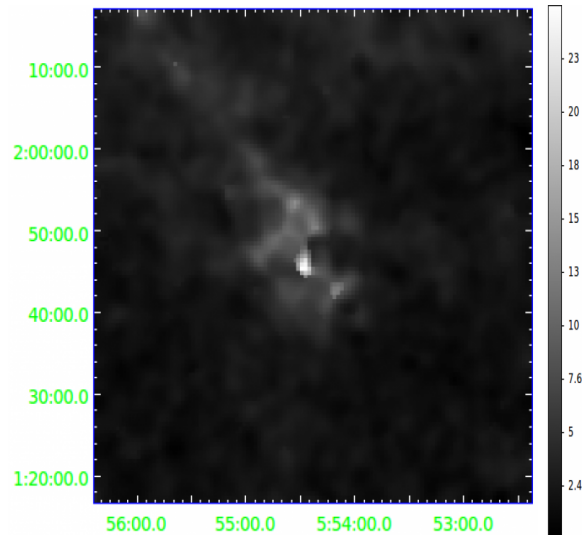


Figure 3.13: Extinction map of LDN1622, produced by 2MASS NICER. The actual size of the pixel is approximately 0.7 times the FWHM, so we have about 1.4 arcmin per pixel. Source: Our work.

3.4 A model of the physical and chemical structure of the LDN1622

We modeled the physical and chemical structures of the L1622 by using a 1D astrochemical model. To do so, we ran the Meudon PDR Code (Le Bourlot et al. , 1993) (Le Petit et al. , 2006) (Le Bourlot et al. , 2012). The 1D astrochemical Meudon PDR Code is based on a stationary plane-parallel geometry of gas and dust illuminated by an ultraviolet (UV) radiation field coming from one or both sides of the cloud, our modeling took into consideration both sides. See Figure 3.14. From starting physical and chemical parameters, the code resolves at each point of the cloud the UV radiative transfer and computes the thermal balance at steady state. That grid of isobaric PDR 1.5.2 models (revision 1787) covers photo-dominated regions conditions. Explored parameters are proton density, UV field intensity and size of the clouds. The full grid contains 1372 2-side models where the back side of the cloud is submitted to the ISRF. The chemistry takes into account 222 species, including C and O isotopes, linked by 6243 chemical reaction. No surface reactions are considered excepted for H₂. H₂ formation model takes into account Eley-Rideal and Langmuir-Hinshelwood mechanisms as described in Le Bourlot et al. (2012). These models give access to all quantities computed by PDR 1.5.2 (line intensities, column densities, densities, temperature of gas and grains, ...). We used Mathis expression for the ISRF since it takes into account more precisely near-UV to near-IR components of the ISRF.

Table 3.2 lists the input parameters we adopted from the literature and observations.

Table 3.2: Input parameters for the modelling of the PDR of LDN1622 using the Meudon PDR Code.

Property	Values
Initial density $n_H(cm^{-3})$	10^4
GO observer side (Mathis units)	35000
GO back side (Mathis units)	10
R_v	3.1
$N_H/E(B - V)$	5.8×10^{21}
$m(dust)/m(gas)$	0.01
Extinction curve	Galaxy
ISRF	Mathis
State equation	isobaric thermal balance

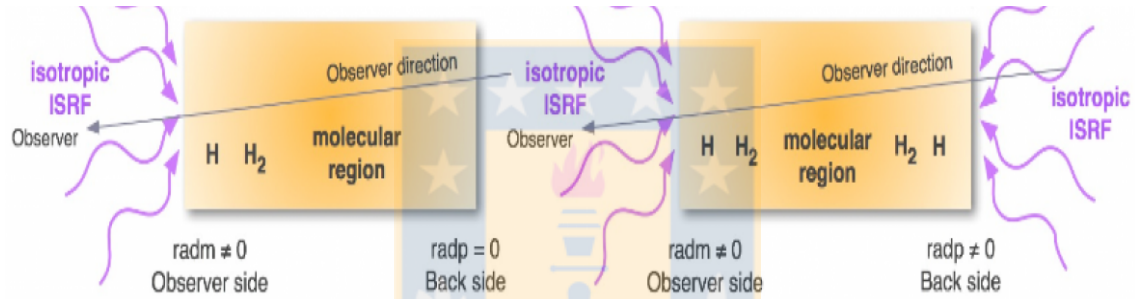


Figure 3.14: Meudon is a model that allows us to simulate the physical conditions of a PDR, is based on a stationary plane-parallel geometry of gas and dust illuminated by an ultraviolet (UV) radiation field coming from one or both sides of the cloud. In the left case, $radp = 0$ to not add the ISRF on the back side.

With these parameters we have worked with two models, one with maximum extinction equal to 10 [mag] and another with maximum extinction equal to 30 [mag]. For the model of $A_{v,max} = 30[mag]$ we have to the Figure 3.15, where in order to analyze the physical structure of LDN1622 we plot the gas state, specifically, the proton density and the total density of the gas. Also gas and dust temperature they were graphed, see Figure 3.15. The MEUDON PDR Code, indicate that the total density is approximately constant to $A_v > 5$. When $A_v < 4$ the gas temperature is higher than dust temperature, but in inner regions the UV flux is blocked up therefore temperatures either gas or dust decrease. The degree of ionization describes a curve similar to the temperature of the gas.

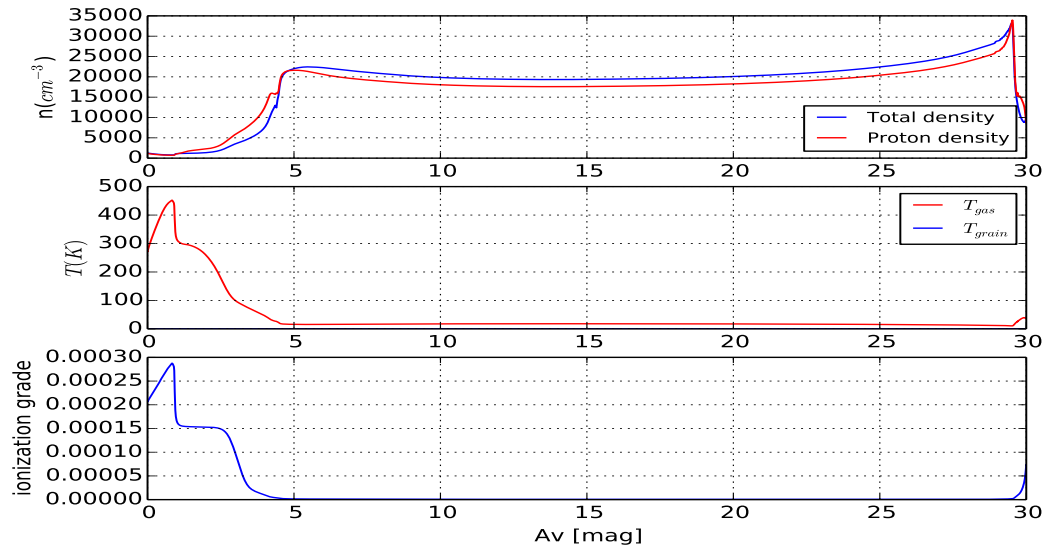


Figure 3.15: All panels are represented as function of the visual extinction, A_v . The first panel shows the proton density ($n(\text{H})+n(\text{H}_2)+n(\text{H}^+)$) and the total density ($n(\text{H})+n(\text{H}_2)+n(\text{He})$), both quantities become constant for high visual extinctions. The second panel represents the grain and gas temperature profiles. The blue area covers the range of dust temperature given by the MEUDON PDR Code for different grain size values in the range 0.03 to $0.3 \mu\text{m}$. The third graph shows how the degree of ionization of the molecules varies depending on the extinction. Source: Our work.

To determine the PDR of L1622, we plot $N(\text{CO})$, $N(\text{C})$, $N(\text{C}^+)$, See Figure 3.16. Given that $N(\text{C})$ is a tracer of PDR, we try to estimate to which visual extinction it is probable to find this species.

The second model that we consider $A_{v_{\text{max}}} = 10[\text{mag}]$. We extract the same graphs as the model with $A_v = 30[\text{mag}]$. In Figure 3.17 we see the state of the gas, temperature of the gas, temperature of the dust grains, and the degree of ionization. And in Figure 3.18 it is possible to see the densities of columns and volumetric densities of C^+ , C and CO , as in the model where we used $A_{v_{\text{max}}} = 30[\text{mag}]$.

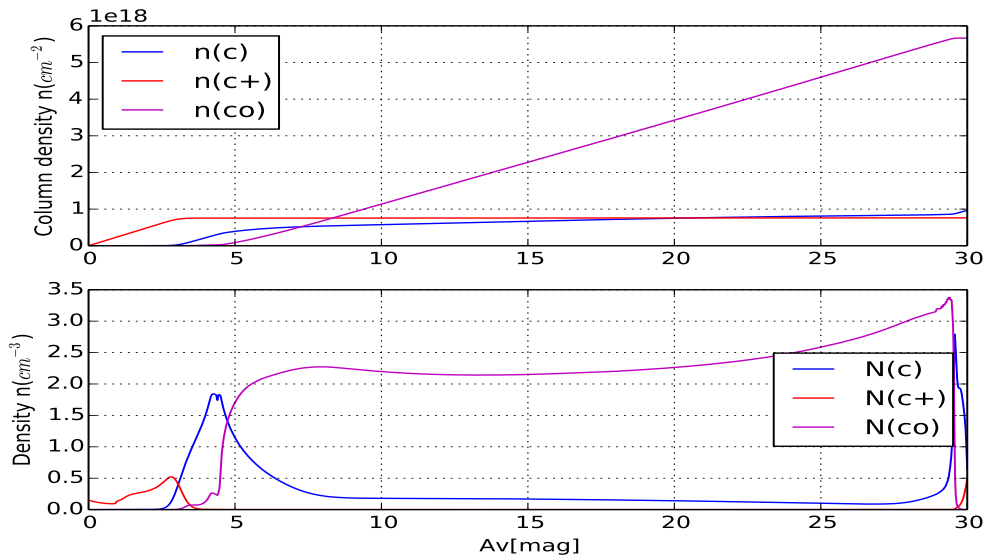


Figure 3.16: The behavior of these 3 molecules was extracted from the Meudon model. In the graph above it shows the density of columns depending on the extinction. Around $A_v = 5$ the formation of CO is noted, but the abundance of C is even greater. For $A_v = 7$ the column density of CO is much greater than C, and almost equal to that of C+. Although for even greater extinctions the column density is much higher than the other two species, it is important to note that the column density of C continues to increase slowly while extinction increases. In the graph above we have the volumetric densities of the same chemical species. Precisely where C+ is decreasing and CO increasing, we find a peak in abundance of C, around $A_v = 4$. Source: Our work.

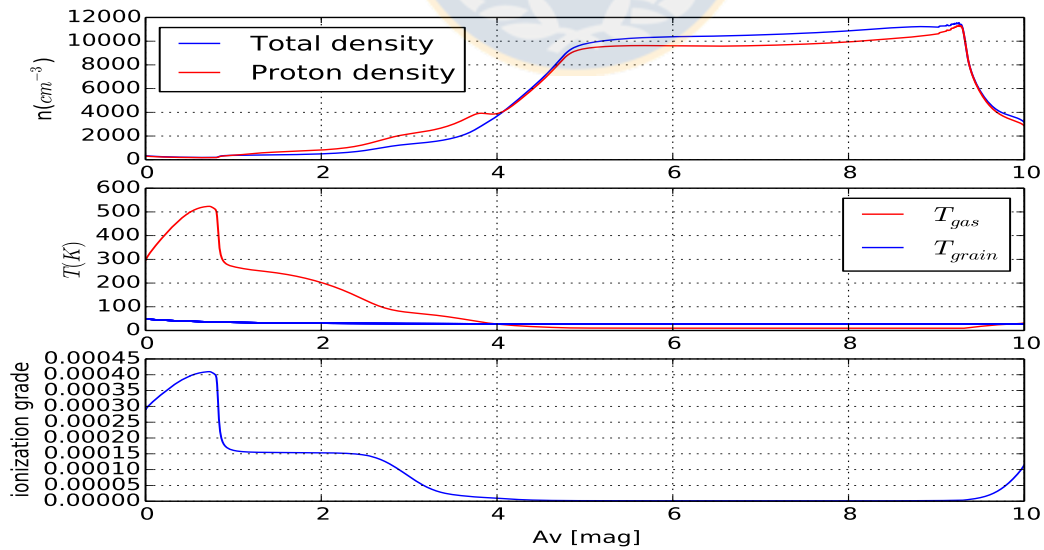


Figure 3.17: The same as Figure 3.15, but with $A_{v_{max}} = 10[mag]$. Source: Our work.

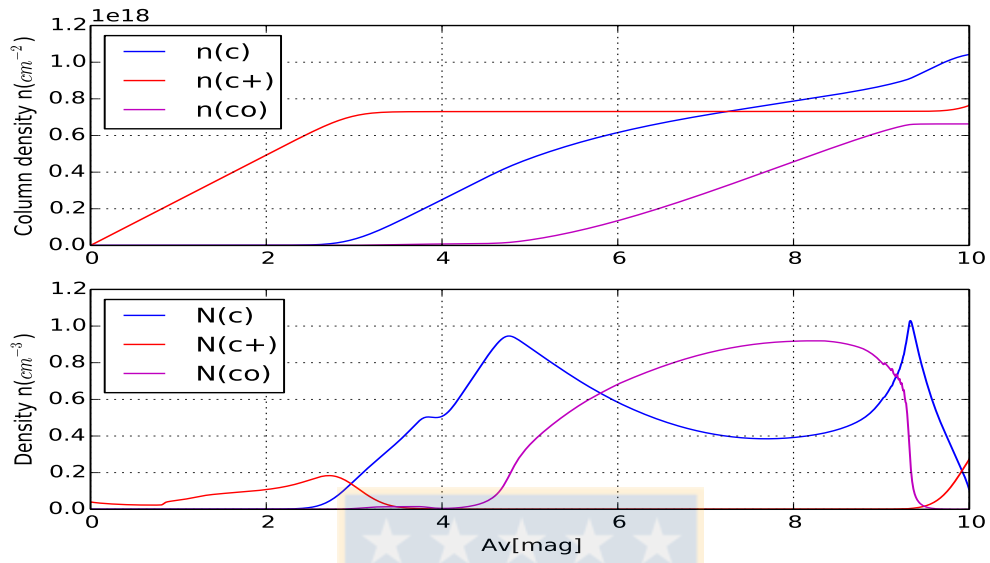


Figure 3.18: The same as Figure 3.16, but with $A_{v_{max}} = 10[mag]$. Source: Our work.

Chapter 4

Conclusion and Discussion

From observations (See Figure 3.11) and the Meudon model (See Figures 3.16 and 3.17), you can see that CI abundance increases when the density of the cloud increases. In the case of Figure 3.16 this increment is smooth, and it can be easily appreciated that it has an almost homogeneous distribution in the region of interest. However in both grills, for extinctions between 3 and 5 we can find an area where C is greater than the CO and C+. It is in this region where we can expect molecular dissociation, PDR, to occur. Along with that, the CO begins to be predominant with respect to C and C+ (for $A_V \approx 5$) and H_2 with respect to H, so it is expected that at higher extinction values there will be regions formed mainly by molecules, as can be seen in Figures 3.8, 3.9, 3.12. Using the extinction map obtained with 2MASS-NICER, the extinction limits will be demarcated where it would be expected to find the PDR, ie. visual extinction between 3 and 5. See Figure 4.1.

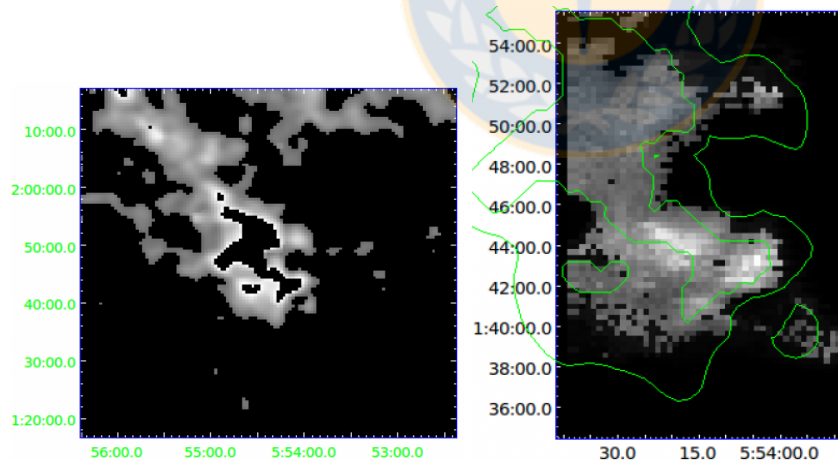


Figure 4.1: Left: Extinction map of LDN1622, all regions with magnitudes less than 3 and greater than 5 were eliminated. Right: Column density map of LDN1622, with contours that delimit visual extinctions between 3 and 5 magnitudes, obtained directly from the image above. The region between these limits is the probable PDR area. Source: Our work.

From the maps of Figure 3.10 we can see the densest areas. However from the map of $C^{18}O$ the small agglomerations of LDN1622 are identified. Map of $C^{13}O$ has the advantage over map ^{12}CO because it is more optically thin, so we can identify deeper regions. According to (Viscuso & Chernoff, 1988) $CO(4-3)$ traces warm (50[K]) and dense ($10^5 cm^{-3}$) nuclei; while $CI(P_1 - P_0)$ requires a minimum excitation temperature of 24[K] and a density of $10^3 cm^{-3}$, due to collisions with H_2 (Schroder et al., 1991).

Previous galactic observations show that ^{12}CO and CI are well related together with ^{13}CO , in J(1-0) and J(2-1) transitions. (Stutzki et al., 1988) suggests that this effect results from the agglomeration of material in a molecular state within a molecular cloud, so that CI is distributed in outer layers. However, the models have not been satisfactory enough to explain the uniformity of the CI found observationally. And it is remarkable that this occurs, since $CO(4-3)$ and CI require very different excitation temperatures and critical densities. One possibility is attributed to the fact that the ISM is lumpy, therefore the UV radiation manages to penetrate the internal areas of the cloud. According to (Kaufman et al., 1999) CI is insensitive to the radiation field. When we take the average in intensities of CI and $CO(4-3)$, we see that $I_{CI}/I_{CO} \approx 1$, this implies that the cloud must have a density less than $10^5 [cm^{-3}]$, which agrees with (Harper et al., 2015).

LDN1622 was observed by Hershel at 160, 250, 350 and 500 [μm]; these wavelengths traces zones of high densities. Specifically we can expect that at 250, 350 and 500 [μm] the maps doesn't show significant differences. From Figure 4.2, it is possible to see the density map of the column with the contours at 160, 250, 350 and 500 [μm] observed by Hershel. As expected, the contours show morphologies very similar to that of the column density map.

It is important to note that in this work, the PDR area of LDN1622 was estimated from a joint analysis between a density map and an extinction map. To determine a map of column density from molecular gas has its advantages and disadvantages with respect to other methods, (Pineda et al., 2008), ^{13}CO is able to be observed in more internal areas of the cloud, which is adversely affected by the optical depth. Other ways to estimate molecular density is using dust, which is expected to have differences with our analysis because in general they do not trace the same portions along some line of sight, nevertheless the study of the gas the study with the dust entails a greater dynamic range. When gas is used, it is difficult to determine a specific density range in which a specific line is possible, which leads to associated errors, but the great advantage of gas over other methods is that it allows studying the kinematics through a line of sight.

The CO column density found in our observations, see Figure 3.10, is in agreement with the CO column density found by the MEUDON model, see Figures 3.18 and 3.16. The same is true for the molecular gas column density (H_2). From our observations, see Figure 3.10, we obtain on average a column density close to 2.5×10^{21} , while the results of the models show an average of 3×10^{21} for visual extinctions greater than 5 magnitudes. It was to be expected that when introducing the same parameters except one to the MEUDON model, the behavior would be similar.

In spite of the multiple approaches, such as not considering all the isotopes of C and O that can make up the CO molecule, nor all of its transitions. The column density results of the molecular gas were very close to those obtained by the Meudon model. As future work it would be important

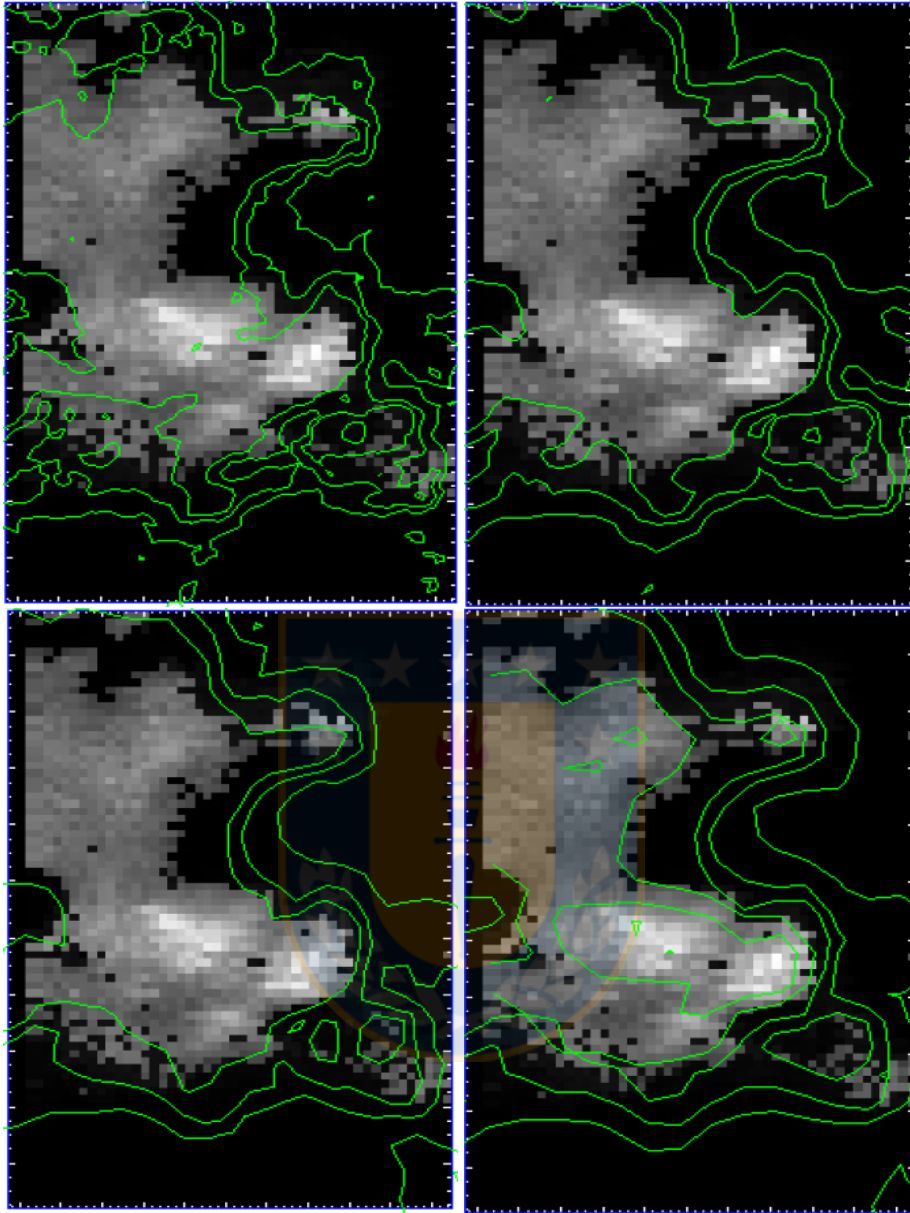


Figure 4.2: The figure shows the map of column density calculated in this work. Top-left: Contours at $160[\mu m]$. Top-right: Contours at $250[\mu m]$. Bottom-left: Contours at $350[\mu m]$. Bottom-right: Contours at $500[\mu m]$. Source: Our work.

to compare the PDR area found here, with molecular gas, with other methods. It can also compare maps in the microwave range, close to 30 [GHz], with the PDR area found in this thesis work.

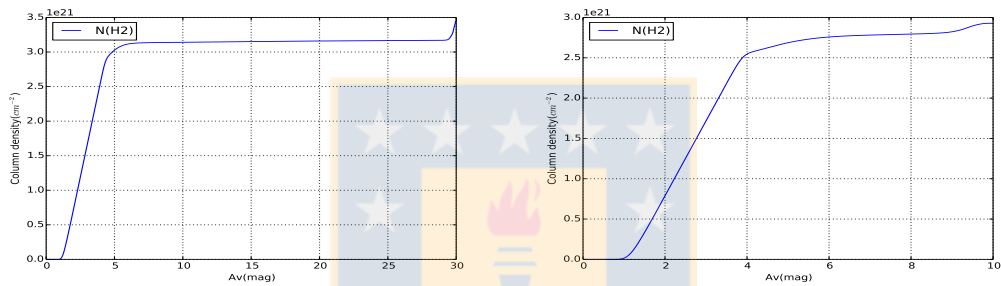


Figure 4.3: Density of the H_2 column obtained from the Meudon model, both have the same input parameters, the only difference is that the graph on the left results from considering a maximum visual extinction of 30 magnitudes and the one on the right considers a maximum visual extinction of 10 Magnitudes. Both results show a maximum column density around 3×10^{21} . Source: Our work.

Bibliography

- Y. Ali-Haïmoud, C. M. Hirata, and C. Dickinson, A refined model for spinning dust radiation, *Monthly Notices of the Royal Astronomical Society*, vol. 395, no. 2, pp. 10551078, 2009.
- Bally, J., Stark, A. A., Wilson, R. W., & Langer, W. D. 1987, *ApJ*, 312, L45
- Bally J., Walawender J., Reipurth B. and Megeath S. T. 2009 *AJ* 137 3843
- E. S. Battistelli, E. Carretti, P. de Bernardis, and S. Masi, "Large Radio Telescopes for Anomalous Microwave Emission Observations," *Advances in Astronomy*, vol. 2012, Article ID 607384, 8 pages, 2012. doi:10.1155/2012/607384
- C. L. Bennett, M. Halpern, G. Hinshaw et al., "First-year wilkinson microwave anisotropy probe (WMAP) observations: preliminary maps and basic results," *The Astrophysical Journal Supplement Series*, vol. 148, no. 1, pp. 127, 2003.
- F. Boulanger and M. Perault, "Diffuse infrared emission from the galaxy. Isolar neighborhood," *The Astrophysical Journal*, vol. 330, pp. 964985, 1988.
- Boulanger, F., Abergel, A., Bernard, J.-P., et al. 1996, *A&A*, 312, 256
- Brown, A. G. A., de Geus, E. J., & de Zeeuw, P. T. 1994, *A&A*, 289, 101.
- Bruce T. Draine(2011), *Physics of the interstellar and Intergalactic medium*, Published by Princeton University Press, 41 William Street, New Jersey 08540
- Casassus, S., Cabrera, G. F., Förster, F., et al. 2006, *ApJ*, 639, 951
- Casassus, S., Dickinson, C., Cleary, K., et al. 2008, *MNRAS*, 391, 1075
- Castellanos, P., Casassus, S., Dickinson, C., et al. 2011, *MNRAS*, 411, 1137
- Correia, S., Zinnecker, H., Ratzka, Th., Sterzik, M. F. 2006, *A&A*, 459, 909
- Davies, R. D., Dickinson, C., Banday, A. J., et al. 2006, *MNRAS*, 370, 1125
- A. De Oliveira-Costa, A., Kogut, A., Devlin, M. J., et al. 1997, *ApJ*, 482, L17.
- de Oliveira-Costa, A., Tegmark, M., Page, L., & Boughn, S. 1998, *ApJ*, 509, L9.
- de Oliveira-Costa, A., et al. 1999, *ApJ*, 527, L9.

- C. Dickinson, R. D. Davies, R. J. Davis; Towards a freefree template for CMB foregrounds, *Monthly Notices of the Royal Astronomical Society*, Volume 341, Issue 2, 11 May 2003, Pages 369384, <https://doi.org/10.1046/j.1365-8711.2003.06439.x>
- Dickinson, C., Davies, R. D., Bronfman, L., et al. 2007, *MNRAS*, 379, 297
- Dickinson C. et al., 2010, *MNRAS*, 407, 2223
- Clive Dickinson, Roberta Paladini, and Laurent Verstraete, Anomalous Microwave Emission: Theory, Modeling, and Observations, *Advances in Astronomy*, vol. 2013, Article ID 134979, 1 pages, 2013. doi:10.1155/2013/134979
- B. T. Draine and A. Lazarian, "Electric dipole radiation from spinning dust grains," *Astrophysical Journal Letters*, vol. 508, no. 1, pp. 157179, 1998.
- B. T. Draine and A. Lazarian, "Magnetic dipole microwave emission from dust grains," *Astrophysical Journal Letters*, vol. 512, no. 2, pp. 740754, 1999.
- B. T. Draine, "On the submillimeter opacity of protoplanetary disks," *The Astrophysical Journal*, vol. 636, no. 2, pp. 11141120, 2006.
- P. J. Encrenaz, "A new source of intense molecular emission in the rho ophiuchi complex," *The Astrophysical Journal*, vol. 189, p. L135, 1974.
- S. Fernández-Cerezo, C. M. Gutierrez, R. Rebolo et al., "Observations of the cosmic microwave background and galactic foregrounds at 1217 [GHz] with the COSMOSOMAS experiment" *Monthly Notices of the Royal Astronomical Society*, vol. 370, no. 1, pp. 1524, 2006.
- Finkbeiner D.P., 2004, *ApJ*, 614, 186
- Finkbeiner, D. P., Schlegel, D. J., Frank, C., & Heiles, C. 2002, *ApJ*, 566, 898
- Gaustad, J. E., McCullough, P. R., Rosing, W. & Van Buren, D. 2001, *PASP*, 113, 1326
- Génova-Santos, R., Rebolo, R., Rubiño-Martín, J. A., López-Caraballo, C. H., & Hildebrandt, S. R. 2011, *ApJ*, 743, 67
- Genzel, R., Harris, A. I., Stutzki, J., and Jaffe, D. T. 1988, *ApJ*, 332, 1049.
- Griffin M. J. et al., 2010, *A&A*, 518, L3
- Guo, Z., Burrows, D. N., Sanders, W. T., Snowden, S. L., & Penprase, B. E. 1995, *ApJ*, 453, 256
- S. E. Harper, C. Dickinson, K. Cleary; Observations of freefree and anomalous microwave emission from LDN 1622 with the 100 m Green Bank Telescope, *Monthly Notices of the Royal Astronomical Society*, Volume 453, Issue 4, 11 November 2015, Pages 33753385, <https://doi.org/10.1093/mnras/stv1863>
- Heiles, C., Haffner, L.M., Reynolds, R.J., Tufte, S.L., 2000, *ApJ*, 536, 335
- G. H. Herbig and K. R. Bell, *cels.book*, 1988.
- G. H. Herbig and K. R. Bell, *cels.book*, 1988.

- Herbig, G. H., & Kameswara Rao, N. 1972, *ApJ*, 174, 401.
- R. H. Hildebrand, "The determination of cloud masses and dust characteristics from submillimetre thermal emission", *Quarterly Journal of the Royal Astronomical Society*, vol. 24, pp. 267282, 1983.
- S. R. Hildebrandt, R. Rebolo, J. A. Rubiño-Martín et al., "COSMOSOMAS observations of the cosmic microwave background and Galactic foregrounds at 11 GHz: evidence for anomalous microwave emission at high Galactic latitude," *Monthly Notices of the Royal Astronomical Society*, vol. 382, no. 2, pp. 594608, 2007.
- Hoang, T., Draine, B. T., & Lazarian, A. 2010, *ApJ*, 715, 1462
- Hoang, T., Lazarian, A., & Draine, B. T. 2011, *ApJ*, 741, 87
- Thiem Hoang and A. Lazarian, "Spinning Dust Emission from Wobbling Grains: Important Physical Effects and Implications," *Advances in Astronomy*, vol. 2012, Article ID 208159, 14 pages, 2012. doi:10.1155/2012/208159
- Kaufman, M.J., Wolfire, M.G., Hollenbach, D.J., & Luhman, M.L. 1999, astro-ph/9907255
- Kirk, H., Di Francesco, J., Johnstone, D., et al. 2016, *ApJ*, 817, 167
- Knude, J., Fabricius, C., Høg, E., & Makarov, V. 2002, *A&A*, 392, 1069
- C. A. Kulesa, A. L. Hungerford, C. K. Walker, X. Zhang, and A. P. Lane, "Large-scale CO and [C I] emission in the rho ophiuchi molecular cloud," *The Astrophysical Journal*, vol. 625, no. 1, pp. 194209, 2005.
- M. Kun, Z. Balog, N. Mizuno et al., "Lynds 1622: a nearby star-forming cloud projected on Orion B?" *Monthly Notices of the Royal Astronomical Society*, vol. 391, pp. 8494, 2008.
- Le Bourlot, J., Pineau Des Forets, G., Roue ff, E., & Flower, D. R. 1993, *A&A*, 267, 233
- Le Bourlot, J., Le Petit, F., Pinto, C., Roue ff, E., & Roy, F. 2012, *A&A*, 541, A76
- Lee, C.W., Myers, P. C., Tafalla, M., 2001, *ApJS*, 136, 703
- Leitch, E. M., Readhead, A. C. S., Pearson, T. J., & Myers, S. T. 1997, *ApJ*, 486, L23
- Le Petit, F., Nehm, C., Le Bourlot, J., & Roue
- Lombardi, M., & Alves, J. 2001, *A&A*, 377, 1023
- D. Lommen, C. M. Wright, S. T. Maddison et al., Investigating grain growth in disks around southern T Tauri stars at millimetre wavelengths, *Astronomy & Astrophysics*, vol. 462, pp. 211220, 2007.
- Maddalena, R. J., Morris, M., Moscowitz, J., & Thaddeus, P. 1986, *ApJ*, 303, 375
- B. S. Mason, T. Robishaw, C. Heiles, D. Finkbeiner, and C. Dickinson, "A limit on the polarized anomalous microwave emission of lynds 1622," *Astrophysical Journal Letters*, vol. 697, no. 2, pp. 11871193, 2009.

- J. S. Mathis, W. Rumpl, and K. H. Nordsieck, "The size distribution of interstellar grains", *The Astrophysical Journal*, vol. 217, pp. 425433, 1977.
- Megeath, S. T., Gutermuth, R., Muzerolle, J., et al. 2012, *AJ*, 144, 192
- Nakano, M., Wiramihardja, S. D., & Kogure, T. 1995, *PASJ*, 47, 889
- Ogura, K., Hasegawa, T. 1983, *PASJ*, 35, 299
- Tibbs C. T., Watson R. A., Dickinson C. et al., 2010, *MNRAS*, 402, 1969
- A. De Oliveira-Costa, M. Tegmark, R. D. Davies et al., "The quest for microwave foreground X," *Astrophysical Journal Letters*, vol. 606, no. 2, pp. L89L92, 2004.
- Pineda, J. E., Caselli, P. & Goodman, A. A. 2008, *ApJ*, 679, 481
- Pineda, J., Goldsmith, P., & Chapman, N. et al. 2010, *ApJ*, 721, 686
- Poglitsch A. et al., 2010, *A&A*, 518, L2
- Reach, W. T., Dwek, E., Fixsen, D. J., et al. 1995, *ApJ*, 451, 188
- Reipurth, B., Megeath, S. T., Bally, J., & Walawender, J. 2008, in *Handbook of Star Forming Regions*, Vol. I, ed. B. Reipurth (San Francisco, CA: ASP), 782
- Reipurth, B., Megeath, S. T., Bally, J., & Walawender, J. 2008, *The L1617 and L1622 Cometary Clouds in Orion*, ed. B. Reipurth, 782
- Reipurth B., Herbig G., Aspin C., *AJ*, 2010, vol. 139 pg. 1668.
- J. Rodmann, T. Henning, C. J. Chandler, L. G. Mundy, and D. J. Wilner, "Large dust particles in disks around T Tauri stars", *Astronomy & Astrophysics*, vol. 446, no. 1, pp. 211221, 2006.
- L. F. Rodriguez, J. Marti, J. Canto, J. M. Moran, and S. Curiel, "Possible radio spectral indices from inhomogeneous free-free sources," *Revista Mexicana De Astronomia Y Astrofisica*, vol. 25, no. 1, pp. 23229, 1993.
- Rodr guez, L., F., Reipurth, B. 1994, *A&A*, 281, 882
- J. A. Rubiño-Martin, C. H. Lopez-Caraballo, R. Genova-Santos, and R. Rebolo, *Observations of the Polarisation of the Anomalous Microwave Emission: A Review*, *Advances in Astronomy*, vol. 2012, Article ID 351836, 15 pages, 2012. doi:10.1155/2012/351836.
- A. Scaife, D. A. Green, R. A. Battye et al., "Constraints on spinning dust towards Galactic targets with the Very Small Array: a tentative detection of excess microwave emission towards 3 C 39 6," *Monthly Notices of the Royal Astronomical Society*, vol. 377, pp. L69L73, 2007.
- A. M. M. Scaife, N. Hurley-Walker, M. L. Davies et al., "AMI limits on 15-GHz excess emission in northern H ii regions," *Monthly Notices of the Royal Astronomical Society*, vol. 385, pp. 809822, 2008.
- A. M. M. Scaife, N. Hurley-Walker, D. A. Green et al., "AMI observations of Lynds dark nebulae: further evidence for anomalous cm-wave emission," *Monthly Notices of the Royal Astronomical Society*, vol. 400, pp. 13941412, 2009.

- A. M. M. Scaife, N. Hurley-Walker, D. A. Green et al., "An excess of emission in the dark cloud LDN1111 with the Arcminute Microkelvin Imager," *Monthly Notices of the Royal Astronomical Society*, vol. 394, pp. L46L50, 2009.
- A. M. M. Scaife, D. A. Green, G. G. Pooley et al., "High-resolution AMI Large Array imaging of spinning dust sources: spatially correlated 8 m emission and evidence of a stellar wind in L675," *Monthly Notices of the Royal Astronomical Society*, vol. 403, pp. L46L50, 2010.
- A. M. M. Scaife, M. Scaife, B. Nikolic et al., "Microwave observations of spinning dust emission in NGC6946," *Monthly Notices of the Royal Astronomical Society*, vol. 406, pp. L45L49, 2010.
- Anna. A. A. Scaife, "Anomalous Microwave Emission from Star Forming Regions" *Advances in Astronomy*, vol. 2013, Article ID 390287, 25 pages, 2013. doi:10.1155/2013/390287.
- Schroder, K., Staemmler, V., Smith, M.D., Flower, D.R., & Jacquet, R. 1991, *J. Phys. B.*, 24, 2487
- Sherry, W. H., Walter, F. M., Wolk, S. J., & Adams, N. R. 2008, *AJ*, 135, 1616
- Silsbee, K., Ali-Haïmoud, Y., & Hirata, C. M. 2011, *MNRAS*, 411, 2750
- K. Silsbee, Y. Ali-Hamoud, and C. M. Hirata, "Spinning dust emission: the effect of rotation around a non-principal axis," *Monthly Notices of the Royal Astronomical Society*, vol. 411, no. 4, pp. 27502769, 2011.
- Stutzki, J., Stacey, G.J., Genzel, R., Harris, A. I., Jaffe, D.T. & Lugten, J.B. 1988, *ApJ*, 332, 379
- H. Tanaka, Y. Himeno, and S. Ida, "Dust growth and settling in protoplanetary disks and disk spectral energy distributions. I. Laminar disks," *Astrophysical Journal Letters*, vol. 625, no. 1, pp. 414426, 2005.
- Tibbs C. T., Watson R. A., Dickinson C. et al., 2010, *MNRAS*, 402, 1969
- Christopher T. Tibbs, Roberta Paladini, and Clive Dickinson, "On the Limitations of the Anomalous Microwave Emission Emissivity," *Advances in Astronomy*, vol. 2012, Article ID 124931, 6 pages, 2012. doi:10.1155/2012/124931
- Tibbs, C. T., Paladini, R., Compiegne, M., et al. 2012a, *ApJ*, 754, 94
- Todorović, M., Davies, R. D., Dickinson, C., et al. 2010, *MNRAS*, 406, 1629
- Vidal, M., Casassus, S., Dickinson, C., et al. 2011, *MNRAS*, 414, 2424
- Viscuso, P.J. & Chernoff, D.F. 1988, *ApJ*, 327, 364
- A. E. Visser, J. S. Richer, and C. J. Chandler, "A SCUBA survey of compact dark Lynds clouds," *Monthly Notices of the Royal Astronomical Society*, vol. 323, no. 2, pp. 257269, 2001.
- Watson R. A., Rebolo R., Rubiño-Martín J. A., Hildebrandt S., Gutiérrez C. M., Fernández-Cerezo S., Hoyland R. J., Battistelli E. S., 2005, *ApJ*, 624, L89
- Wilson, B.A., Dame, T.M., Mashedier, M.R., Thaddeus, P., 2005, *A&A*, 430, 523
- Wiramihardja, S. D., Kogure, T., Yoshida, S., Ogura, K., & Nakano, M. 1989, *PASJ*, 41, 155

Wright E. L. et al., 2010, *AJ*, 140, 1868

Yacine Ali-Hamoud, "Spinning Dust Radiation: A Review of the Theory," *Advances in Astronomy*, vol. 2013, Article ID 462697, 13 pages, 2013. doi:10.1155/2013/462697

K. E. Young, M. L. Enoch, N. J. Evans II et al., "Bolocam survey for 1.1 mm dust continuum emission in the c2d legacy clouds. II. Ophiuchus," *The Astrophysical Journal*, vol. 644, no. 1, article 326, 2006.

N. Ysard, M. A. Miville-Deschênes, and L. Verstraete, "Probing the origin of the microwave anomalous foreground," *Astronomy & Astrophysics*, vol. 509, article L1, 2010.

Ysard, N., & Verstraete, L. 2010, *A&A*, 509, A12

Zhang, X., Lee, Y., Bolatto, A., and Stark, A. A. 2001, *ApJ*, 553, 274



Appendix

This is the script with which the LDN1622 $^{13}\text{CO}(2-1)$ intensity map was generated. Changing the name, intervals of speeds and frequencies in the script can obtain the map of $\text{CO}(2-1)$ and $\text{C}^{18}\text{O}(2-1)$

```

set format l
set plot h
set ang s
set unit v f
set var spec read
file in 12feb2015.cso
find
set mode x auto
set mode y auto
set sou LDN1622C ! set sou LDN1622*

set tele "CSO FFTS 1W"

set range -600 600 -600 600 ! set range -600 600 -600 600

find
set win -580 -550
$rm ldn1622_base18.dat
file out ldn1622_base18.dat m

for i 1 to found
get n
set unit c !
for k 4095.8 to 4098.3 !
draw k k !
next !
set unit v
sm
base 1 /pl
pen 0
pl
!fill 6 16 357 373 534 540 /noise !ESTO NO ESTABA
mod band
mod line C18O2-1
mod freq 219560.358
write
next

file in ldn1622_base18.dat

```



```

find
set unit v
$rm map_18co.tab
print area -5E5 5E5 /output map_c18o.tab !-5 5

clear

!column x 2 y 3 z 4 /file map_12co.tab
!column x 2 y 3 z 4 /file map_13co.tab
column x 2 y 3 z 4 /file map_c18o.tab
levels 2 to 5 by 1
rgdata /blanking -1000
limits /rgdata /reverse x
!set box location -5 5 -5 5
set box match
pl
box
set ang s
pl
box
rgmap /grey
rgmap /per 20
!rgmap
label "RA Offset (arcmin)" /x
label "Dec Offset (arcmin)" /y
wedge

$rm c18o21*
table c18o21 new /math tdv(-5,5) ! -5 5
xy_map c18o21
let name c18o21
let type lmv
go view
go bit
hardcopy ldn1622c18o.png /dev eps color /over
vector\fits ldn1622c18o.fits FROM c18o21.lmv

```

